

**COMPUTATIONAL ANALYSIS OF
ZEL'DOVICH-VON NEUMANN-DOERING (ZND) DETONATION**

A Thesis

by

TETSU NAKAMURA

Submitted to the Office of Graduate Studies of
Texas A&M University
in partial fulfillment of the requirements for the degree of

MASTER OF SCIENCE

May 2010

Major Subject: Aerospace Engineering

**COMPUTATIONAL ANALYSIS OF
ZEL'DOVICH-VON NEUMANN-DOERING (ZND) DETONATION**

A Thesis

by

TETSU NAKAMURA

Submitted to the Office of Graduate Studies of
Texas A&M University
in partial fulfillment of the requirements for the degree of

MASTER OF SCIENCE

Approved by:

Chair of Committee, Adonios N. Karpetis
Committee Members, Kalyan Annamalai
Rodney D. W. Bowersox
Head of Department, Dimitris C. Lagoudas

May 2010

Major Subject: Aerospace Engineering

ABSTRACT

Computational Analysis of
Zel'dovich-von Neumann-Doering (ZND) Detonation. (May 2010)

Tetsu Nakamura, B.S., Texas A&M University

Chair of Advisory Committee: Dr. Adonios N. Karpetis

The Transient Inlet Concept (TIC) involves transient aerodynamics and wave interactions with the objective of producing turbulence, compression and flow in ducted engines at low subsonic speeds. This concept relies on the generation and control of multiple detonation waves issuing from different “stages” along a simple ducted engine, and aims to eliminate the need for compressors at low speeds. Currently, the Zel'dovich-von Neumann-Doering (ZND) steady, one-dimensional detonation is the simplest method of generating the waves issuing from each stage of the TIC device.

This thesis focuses on the primary calculation of a full thermochemistry through a ZND detonation from an initially unreacted supersonic state, through a discontinuous shock wave and a subsonic reaction zone, to the final, reacted, equilibrium state. Modeling of the ZND detonation is accomplished using *Cantera*, an open-source object-oriented code developed at Caltech. The code provides a robust framework for treating thermodynamics, chemical kinetics, and transport processes, as well as numerical solvers for various reacting flow problems. The present work examines the effects of chemical kinetics on the structure of ZND detonation, by using a detailed chemical kinetics mechanism that involves 53 species and 325 simultaneous reactions (Gas Research Institute 3.0). Using a direct integration of the system of inviscid ordinary differential equations for the ZND detonation, I obtain results for the combination of different fuels (hydrogen and methane) and oxidizers (oxygen and air). The detailed thermochemistry

results of the calculations are critically examined for use in a future induced-detonation compression system.

DEDICATION

I dedicate this thesis to my father and mother, Hiroshi and Yuko Nakamura, and to my wife, Noriko Nakamura, for all their patience and understanding as I reached this level of my education.

ACKNOWLEDGEMENTS

I wish to express sincere gratitude to my advisor and committee chair, Dr. Adonios N. Karpetis who has tolerated me for many years and guided me on this educational journey. His guidance gave this project life and gave me the inspiration to complete it.

I would also like to thank the other members of my committee, Dr. Rodney Bowersox and Dr. Kalyan Annamalai, for their advice and support. Their abilities are stellar and stand out in a crowded, and extremely challenging, field.

Financial support of the U.S. Air Force Office of Scientific Research (AFOSR) through grant FA 9950-08-1-0333, (Douglas Smith, manager) is gratefully acknowledged. This opportunity has enabled the completion of this thesis.

I thank my colleagues at Texas A&M for their advice and encouragement. This includes Adam Johnson, Alex Bayeh, Celine Kluzek and Nicole Mendoza.

Finally, I must thank my parents for their steadfast support and encouragement from the beginning, and most importantly, I am exceptionally grateful to my wife Noriko, who endured both time away and distance from me.

NOMENCLATURE

A	Area, m ²
A_k	Pre-exponential Arrhenius constant for reaction k
C_p	Specific heat under constant pressure for mixture, J/kg
$C_{p,i}$	Specific heat under constant pressure for species i , J/kg
$C_{i,react}^{w'}$	Concentration of reactants for species i , mol/m ³
$C_{i,prod}^{w''}$	Concentration of products for species i , mol/m ³
$C_{p,i}^0$	Standard heat capacity under constant pressure of species i at reference temperature
E_k	Activation energy of the forward reaction for reaction k
$\bar{g}_{i,k}^\circ$	Gibbs free energy for species i in reaction k
$\Delta\bar{g}_k^\circ$	Difference of Gibbs free energy for reaction k
h	Specific enthalpy, J/kg
h_i^0	Standard enthalpy of species i at reference temperature, J/kmol
h_i^s	Sensible enthalpy of species i , J/kmol
$h_{f,i}^0$	Enthalpy of formation of species i , J/kmol
$k_{f,k}$	Specific reaction rate constant for forward reaction in reaction k , kmol/(m ³ s)

$k_{b,k}$	Specific reaction rate constant for backward reaction in reaction k , kmol/(m ³ s)
$K_{C,k(T)}$	Equilibrium constant based upon species concentration
$K_{P,k(T)}$	Partial pressure equilibrium constant
M_i	Chemical symbol for species i
MW_i	Molecular weight of species i , kg/kmol
n	Arrhenius pre-exponential temperature exponent
N	Total number of species in a mixture composition
P	Pressure, Pa
$\underline{\underline{P}}$	Pressure tensor
\bar{q}	Heat flux vector
Q	Heat generation through reaction process
\bar{R}	Universal gas constant
R	Specific gas constant
s_i^0	Standard entropy of species i at reference temperature
t	Time, s
T	Temperature, K
u	Fluid velocity in the x -direction, m/s
\bar{V}	Velocity vector, m/s
\bar{V}_i	Diffusion velocity of species i , m/s

V	Specific volume, m^3/kg
v'_i	Stoichiometric coefficient for species i appearing as a reactant
v''_i	Stoichiometric coefficient for species i appearing as a product
$v'_{i,k}$	Stoichiometric coefficients for species i appearing as a reactant in reaction k
$v''_{i,k}$	Stoichiometric coefficients for species i appearing as a product in reaction k
\dot{w}_i	Mass production/destruction rate of species i , $\text{kg}/(\text{m}^3\text{s})$
X_i	Molar fraction of species i
Y_i	Mass fraction of species i

Symbols

γ	Ratio of specific heat
δF	Distributed wall friction per unit flow area
δQ	Distributed heat transfer per unit flow area
ρ	Density, kg/m^3
ω'_k	Progress of reaction variable for reaction k , $\text{kmol}/(\text{m}^3\text{s})$
$\hat{\omega}_{i,k}$	Production or destruction rate of species i in reaction k , $\text{kmol}/(\text{m}^3\text{s})$
$\hat{\omega}_i$	Production or destruction rate of species i , $\text{kmol}/(\text{m}^3\text{s})$

TABLE OF CONTENTS

	Page
ABSTRACT.....	iii
DEDICATION.....	v
ACKNOWLEDGEMENTS.....	vi
NOMENCLATURE	vii
TABLE OF CONTENTS.....	x
LIST OF FIGURES	xii
LIST OF TABLES.....	xv
1. INTRODUCTION.....	1
Transient Inlet Concept.....	1
Single Stage Detonation Generator.....	2
Structure of Zel'dovich-von Neumann-Doering Detonation	4
2. THEORY OF CHEMICALLY REACTING FLOW	6
Conservation Equations	6
Chemical Kinetics for Mass Production/Destruction Rates	8
3. COMPUTATIONAL PROCEDURES.....	11
Cantera Chemically Reacting Flow Program	11
Computational Algorithm.....	11
Rankine-Hugoniot Analysis.....	14
Discontinuous Shock Calculation.....	16
Well-stirred Reactor (WSR)	17

	Page
4. NUMERICAL METHODOLOGY AND STABILITY ANALYSIS	23
Numerical Methodology	23
Limits on Step-size	24
Explicit Versus Implicit Methods and Their Orders	31
Required Computational Time Study	35
5. RESULTS AND ANALYSIS.....	37
H ₂ -O ₂ Reaction Mechanism.....	37
Structure of H ₂ -O ₂ ZND Detonation.....	39
Structure of H ₂ -Air ZND Detonation.....	43
Comparison between Full and Reduced H ₂ -O ₂ Reaction Mechanisms	47
CH ₄ -O ₂ Reaction Mechanism	51
Structure of CH ₄ -O ₂ ZND Detonation	53
Structure of CH ₄ -Air ZND Detonation.....	56
Chapman-Jouguet and Overdriven Detonation on <i>P-v</i> Diagram	60
Mollier Diagrams	62
Differential Area Effect (Diffuser)	65
Future Research	66
6. CONCLUSIONS	68
REFERENCES	69
VITA.....	72

LIST OF FIGURES

FIGURE	Page
1.1 Schematic diagram of transient inlet concept.....	1
1.2 Procedure of detonation generation for a closed tube.....	3
1.3 Schematic diagram of pressure, temperature, density, and velocity in Zel'dovich-von Neumann-Doering detonation.....	4
3.1 Schematic diagram of computing chemically reacting flow by <i>Cantera</i>	13
3.2 Rayleigh line and Hugoniot curves for Chapman-Jouguet methane/oxygen detonation.....	15
3.3 A Well-Stirred Reactor (WSR) model for the computation of a ZND reaction zone	18
3.4 Results of well-stirred reactor model for $A = 1.0 \text{ m}^2$	20
3.5 Results of well-stirred reactor model for $A = 10 \text{ m}^2$	21
3.6 Results of well-stirred reactor model for $A = 100 \text{ m}^2$	22
4.1 Temperature profiles of the $\text{CH}_4\text{-O}_2$ Chapman-Jouguet (CJ) detonation using different step-sizes	25
4.2 Mass fraction of methane molecules using different step-sizes, legend as in Figure 4.1	26
4.3 Detail from Figure 4.2	27
4.4 Mass fraction of hydrogen radicals using different step-sizes, legend as in Figure 4.1	28
4.5 Mass fraction of oxygen radicals using different step-sizes, legend as in Figure 4.1	28
4.6 Mass fraction of CH radicals using different step-sizes, legend as in Figure 4.1	30

FIGURE	Page
4.7 Exposition of the implicit Backward Differential Formula (BDF) scheme	32
4.8 Qualitative description of a stiff Ordinary Differential Equation problem	33
4.9 Errors between explicit Euler and implicit Backward Differential ODEs solutions	34
4.10 Total computational time for different step-sizes	35
5.1 Thermodynamic properties and velocity of the ZND detonation (Initial P : 1 atm, T : 300 K, M : 5.3)	40
5.2 Temperature and species mass fractions in the reaction zone	42
5.3 The CJ detonation of hydrogen/oxygen and hydrogen/air mixture	43
5.4 P - v diagrams of hydrogen/oxygen and hydrogen/air detonations	45
5.5 Mass fraction of NO and temperature for a hydrogen/air detonation.....	47
5.6 $2\text{H}_2 + \text{O}_2 + 9\text{Ar}$ CJ detonation: GRI 3.0 reaction mechanism compared to KIN reaction mechanism	48
5.7 OH mole fraction for LASL and GRI kinetic mechanisms in a reaction zone	50
5.8 Mass production/destruction rates of CJ $\text{CH}_4\text{-O}_2$ detonation	52
5.9 Pressure contour for the CJ detonation of stoichiometric $\text{CH}_4\text{-O}_2$ reaction (Initial P : 1 atm, T : 300 K)	53
5.10 Temperature and mass fractions of main species in the reaction zone for the CJ detonation of stoichiometric $\text{CH}_4\text{-O}_2$ mixture (Initial P : 1 atm, T : 300 K)	54
5.11 Velocity, sound speed, and Mach number in the reaction zone for the CJ detonation of stoichiometric $\text{CH}_4\text{-O}_2$ mixture (Initial P : 1 atm, T : 300 K)	55
5.12 The CJ detonation of methane/oxygen and hydrogen/air mixture.....	56

FIGURE	Page
5.13 P - v diagrams of methane/oxygen and methane/air detonations	58
5.14 Mass fraction of NO and temperature for a methane/air detonation	60
5.15 The CJ detonation of $\text{CH}_4\text{-O}_2$ reaction on a Rankine-Hugoniot diagram.....	61
5.16 Schematic diagram of over-driven detonation by a piston	61
5.17 Comparison between an overdriven detonation ($M_{CJ} = 1.2$) and a Chapman-Jouguet detonation ($M_{CJ} = 1.0$) in P - v diagram.....	62
5.18 The Mollier diagram (h - s) of a $\text{CH}_4\text{-O}_2$ Chapman-Jouguet detonation	63
5.19 Temperature-Entropy diagram of a $\text{CH}_4\text{-O}_2$ Chapman-Jouguet detonation	64
5.20 Chapman-Jouguet detonation through a diffuser	65
5.21 Pressure change using different diffuser cross-sectional areas.....	66

LIST OF TABLES

TABLE	Page
5.1 Possible reaction mechanism of H ₂ -O ₂	38
5.2 Pressure differences between an experimental and calculated result	41
5.3 Comparison of physical properties between H ₂ -O ₂ and H ₂ -Air Detonation, no equivalent accuracy should be inferred	44
5.4 Details of thermal NO _x reaction mechanism.....	46
5.5 Reaction mechanism of LASL program for H ₂ -O ₂ -Ar reaction	49
5.6 Main reactions and mechanism of methane/oxygen combustion	52
5.7 Comparison of physical properties between CH ₄ -O ₂ and CH ₄ -Air Detonation, no equivalent accuracy should be inferred.....	57
5.8 Details of prompt NO _x reaction mechanism	59

1. INTRODUCTION

Transient Inlet Concept

Conventional jet engines operating under the Brayton cycle require rotational compressors to increase the air pressure flowing through the engine [1]. These compressors, in turn, need to be powered by turbines that further contribute to the complexity of the engine. The compressor is not the only device that can increase air pressure through the engine: as the air is slowed down in the diffuser, its static pressure increases through the ram effect. As the air speed increases to supersonic values, compression through the ram effect becomes comparable to, and sometimes exceeds, the pressure increase through the compressor. This allows for the construction of simple ducted engines (ramjets) that require no compressor or turbine to operate. It is important to note that a ramjet does not operate on its own, since the ramjet needs some other device to accelerate it to supersonic speed.

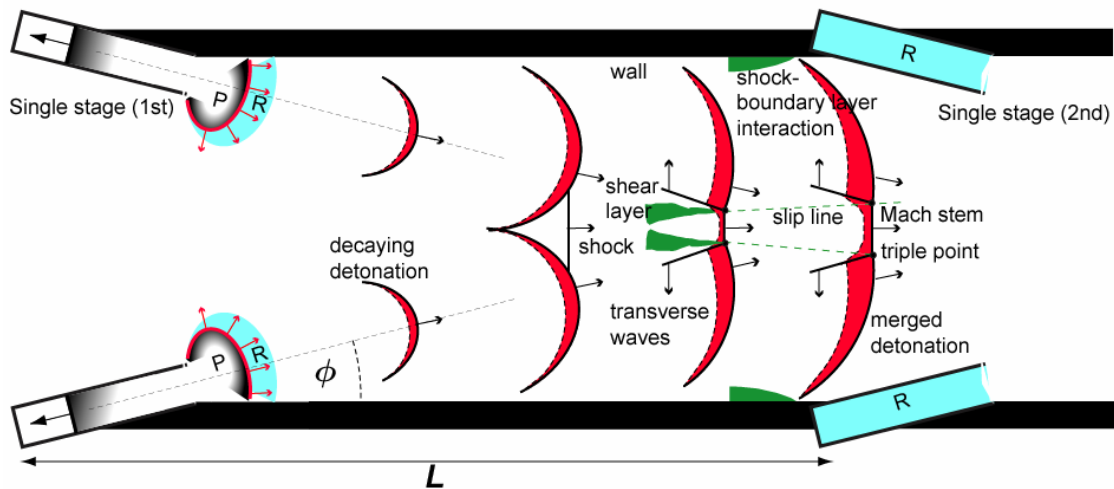


Figure 1.1. Schematic diagram of transient inlet concept

This thesis follows the style and format of the Journal of Turbomachinery.

This research is part of a multi group work assembled in order to design and build a transient inlet device, which is meant to mimic the simplicity of the ramjet operation, even at low subsonic speeds (see Figure 1.1). A transient inlet concept aims to produce flow induction, turbulence generation, and flow compression. All three aspects are necessary before the main fuel and air input into the device, i.e. the transient inlet is supposed to fulfill these goals and not act as a thrust generating device.

The transient inlet concept operates through the interaction and merging of multiple detonations, therefore it requires the presence of multiple stages of detonation generators. Each single stage is a small scale detonation tube, and the individual stages are arranged symmetrically as shown in Figure 1.1. After ignition in each tube a deflagration (slow flame) ensues which transitions to a Chapman-Jouguet (CJ) detonation wave after a required induction time/length. A decaying detonation wave propagates into the main duct, as shown in Figure 1.1, until it meets and interacts with the wave issuing from the opposite generator. When two detonation waves interact in the main tube, a Mach stem is formed by the interaction of the regular and transverse wave fronts. Triple points appear at the intersections of these three waves, and the transverse waves move toward the wall of the main tube. Behind the triple points, the flow is separated by a slip line into two layers with different velocities. This velocity difference induces a turbulent flow behind the merged detonation wave. When the edge of the detonation wave reaches the tube wall, a shock-boundary interaction ensues, the boundary layer grows behind the wave, and additional turbulence is generated within the tube (all shown in Figure 1.1).

Single Stage Detonation Generator

The present research focuses on the computation of a single-stage detonation within one of the injectors shown in Figure 1.1. Figure 1.2 schematically describes the procedure of single detonation wave propagation. A detonation generator is an unsteady propulsive

device in which the combustion chamber is periodically filled with a reactive gas mixture, a detonation is initiated, the detonation propagates through the tube, and the product gases are exhausted [2, 3]. At first, the ignition induces a deflagration wave at the end of the closed tube. Since the closed tube is filled with unburnt reactants, the deflagration velocity increases and a deflagration-to-detonation transition (DDT) occurs during the wave propagation [4, 5, 6, 7]. A deflagration-to-detonation transition is the general process by which a subsonic combustion wave (deflagration) becomes a supersonic combustion wave (detonation). A steady detonation wave propagates along the tube by consuming the premixed unburnt mixture and pushes out unburnt reactants into the main device. The detonation reaches the end of the tube and propagates outward into the surroundings as a shock. If enough unburnt premixture remains in the surroundings, the detonation wave may still propagate as a supersonic shock front followed by a reaction zone, i.e. as a decaying detonation, as shown in Figure 1.2.

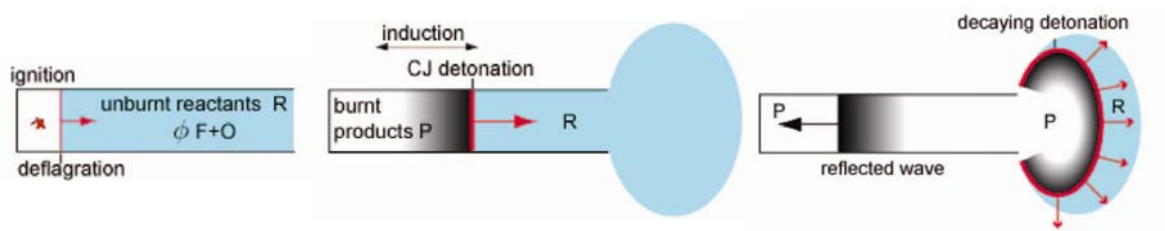


Figure 1.2. Procedure of detonation generation for a closed tube

This study examines in detail the steady state propagation of a Chapman-Jouguet (CJ) detonation as shown in the middle of Figure 1.2. The work computes the CJ detonation by using a detailed chemistry computer code (Cantera) to calculate the transient behavior behind the leading shock.

Structure of Zel'dovich-von Neumann-Doering Detonation

The simplest description of a detonation structure was developed by Zel'dovich [8], von Neumann [9], and Doering [10] independently in the 1940s. They considered a detonation as consisting of two parts: a leading shock wave compressing the unburnt reactants, and a chemical reaction zone that follows the shock after some distance and completes the conversion to products. The shock region is assumed to be infinitesimally thin, and the mixture composition does not change through the discontinuous shock wave. Thermodynamic properties change due to the shock compression effect. As a result, when the unburnt reactant flow passes through the shock, the pressure, density, and temperature increase, while the fluid velocity decreases to a subsonic value, following the usual normal shock relations [11].

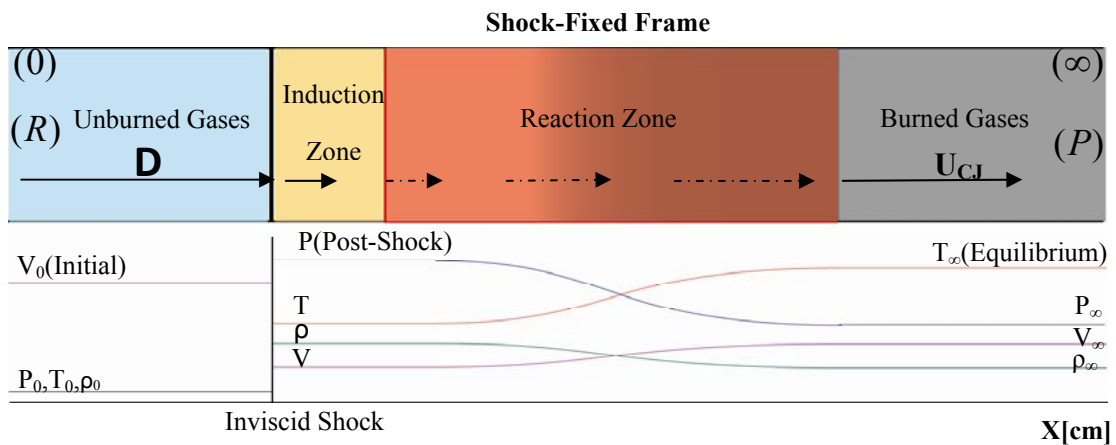


Figure 1.3. Schematic diagram of pressure, temperature, density, and velocity in Zel'dovich-von Neumann-Doering detonation

The ZND detonation is a planar one dimensional structure with no transport effects, such as heat conduction, radiation, mass diffusion, and viscosity [12]. Figure 1.3 qualitatively shows the behavior of pressure, temperature, density, and velocity throughout the entire

process of a steady ZND detonation. First, an incoming unburnt reactant mixture, whose velocity is equal to the supersonic shock velocity (D), is compressed by the inviscid shock. Pressure increases discontinuously to its maximum value due to shock compression, and velocity behind the shock wave takes subsonic values. Then, the pressure gradually decreases to its equilibrium condition because of flow expansion through the reaction zone. Temperature also increases due to the shock compression, however, temperature continues to increase through the reaction zone due to the heat release associated with the reaction. The subsonic velocity in the reaction zone increases to its equilibrium state ($V_{\infty} = U_{CJ}$), which can be shown to coincide with the local sonic condition. The velocity behavior induces the inverse effect on density because of the one dimensional nature of the problem, and the constancy of mass flux ($\rho u = \text{constant}$).

2. THEORY OF CHEMICALLY REACTING FLOW

This section presents the steady one dimensional Zel'dovitch-von Neumann-Doering model and provides the fundamental equations of thermochemistry and chemical kinetics. Particular emphasis is placed on the chemical source terms that are calculated in every step of the solution of the premixed one-dimensional detonation.

Conservation Equations

The conservation laws of mass, momentum, energy, and species for the reactive mixture with transport effects, i.e. the reactive Navier-Stokes equations [13], are:

$$\begin{aligned}\frac{\partial \rho}{\partial t} + \nabla \cdot (\rho \vec{V}) &= 0 \\ \rho \left(\frac{\partial \vec{V}}{\partial t} + \nabla \cdot \vec{V} \right) &= \nabla \cdot \underline{\underline{P}} \\ \rho \frac{\partial (h - P/\rho)}{\partial t} + \rho \vec{V} \cdot \nabla (h - P/\rho) &= -\nabla \cdot \vec{q} - \underline{\underline{P}} : (\nabla \cdot \vec{V}) \\ \rho \frac{\partial Y_i}{\partial t} + \nabla \cdot (\rho \vec{V} Y_i) + \nabla \cdot (\rho Y_i \vec{V}_i) &= \dot{w}_i\end{aligned}$$

where ρ is a fluid density, \vec{V} is a mass-average velocity of gas mixture, $\underline{\underline{P}}$ is the stress tensor, P is the pressure of the gas mixture, h is the specific enthalpy of the gas mixture which includes both sensible and formation components, \vec{q} is a heat flux vector, and \vec{V}_i is the diffusion velocity, Y_i is the mass fraction, and \dot{w}_i is the mass production/destruction rate of species i . Each equation is composed of accumulation (transient), convection, diffusion, and reaction terms. In high speed flow we can assume that the diffusion terms are much smaller than the corresponding convection terms, and therefore the higher order diffusion terms can be eliminated from the above system of differential equations. In steady reactive flow, the accumulation term disappears, while

in the one dimensional case convection is assumed to operate only along the propagating direction x . The one dimensional flow assumption neglects wall boundary effects, which are considered negligible for inviscid flow anyway. Therefore, the equations for a compressible steady one dimensional detonation wave take the simpler forms shown below.

$$\begin{aligned}\frac{d}{dx}(\rho u) &= 0 \\ \frac{d}{dx}(P + \rho u^2) &= 0 \\ \frac{d}{dx}\left(h + \frac{u^2}{2}\right) &= 0 \\ u \frac{dY_i}{dx} &= \frac{\dot{w}_i}{\rho}\end{aligned}$$

where u is fluid velocity in the x -direction. The system of equations is augmented by appropriate equations of state (EOS) for ideal gases:

Thermal equation of state:

$$P = \rho RT$$

Caloric equation of state:

$$h_i = h_i^s + h_{f,i}^o = \int C_{p,i} dT + h_{f,i}^o$$

where h_i^s is the sensible enthalpy, $h_{f,i}^o$ is the enthalpy of formation, and $C_{p,i}$ is the specific heat at constant pressure for each species i , and R is the specific gas constant of mixture. The sensible enthalpy is the thermal energy of mixture, while the formation enthalpy is the chemical energy associated with each species molecule. The specific enthalpy of the mixture can be calculated as:

$$h = \sum_{i=1}^N Y_i h_i$$

where N is the total number of species in the mixture.

The differential form of steady one dimensional reactive flow equations can be integrated under a constant specific heat assumption to provide the following set of integral equations.

$$\rho_1 u_1 = \rho_2 u_2$$

$$p_1 + \rho_1 u_1^2 = p_2 + \rho_2 u_2^2$$

$$h_1 + \frac{1}{2} u_1^2 = h_2 + \frac{1}{2} u_2^2$$

or

$$C_p T_1 + \frac{u_1^2}{2} + Q = C_p T_2 + \frac{u_2^2}{2}$$

$$Q = \left(\sum_{i=1}^N Y_i h_{f,i}^0 \right)_1 - \left(\sum_{i=1}^N Y_i h_{f,i}^0 \right)_2$$

where Q is the heat generation through the reaction process. This last step and the associated assumption of $C_p = \text{constant}$ are not used during the computational solution of the problem. They are presented here solely as an aid to theoretical understanding.

Chemical Kinetics for Mass Production/ Destruction Rates

Some chemical reactions occur very rapidly and others very slowly. All chemical reactions take place at a finite rate that depends on thermochemistry, i.e. pressure and temperature of the mixture, as well as concentrations of the chemical compounds [14].

A one-step elementary chemical reaction can be represented by the following stoichiometric equation

$$\sum_{i=1}^N v_i' M_i = \sum_{i=1}^N v_i'' M_i$$

where ν_i' are the stoichiometric coefficients of the reactants, ν_i'' are the stoichiometric coefficients of the products, and M_i symbolizes the chemical species. Thus, if the species M_i does not appear as a reactant, $\nu_i' = 0$, and if the species M_i does not appear as a product, $\nu_i'' = 0$.

Most elementary reactions follow an Arrhenius law such as

$$k_{f,k} = A_k T^n \exp\left(-\frac{E_k}{RT}\right)$$

where $k_{f,k}$ is the specific reaction rate constant, A_k is the pre-exponential Arrhenius constant, and E_k is the activation energy of the forward reaction k .

The backward reaction rate coefficients ($k_{b,k}$) can be calculated from a relationship of the equilibrium constant to both forward and backward reaction rate coefficients, namely

$$k_{b,k} = \frac{k_{f,k}}{K_{C,k}(T)}$$

$$K_{C,k}(T) = \frac{K_{P,k}(T)}{(\bar{R}T)^{\sum_i (\nu_{i,k}'' - \nu_{i,k}')}} = \frac{\exp\left(-\frac{\Delta\bar{g}_k^\circ}{RT}\right)}{(\bar{R}T)^{\sum_i (\nu_{i,k}' - \nu_{i,k}'')}}}$$

$$\Delta\bar{g}_k^\circ = \sum_i (\nu_{i,k}'' \bar{g}_{i,k}^\circ - \nu_{i,k}' \bar{g}_{i,k}^\circ)$$

where $K_{C,k}$ is the equilibrium constant based on species concentration and $K_{P,k}$ is the partial pressure equilibrium constant. The equilibrium constant for each reaction is related to the difference of molar Gibbs free energy ($\Delta\bar{g}_k^\circ$) between reactants and

products in each reaction as shown in the equation above. Both K_C and K_P are functions of temperature alone.

The progress of reaction variables (ω'_k) can be evaluated as

$$\omega'_k = k_{f,k} \prod_{i=1}^N C_i^{v'_{i,k}} - k_{b,k} \prod_{i=1}^N C_i^{v''_{i,k}}$$

where C_i is the concentration of species i . The rate of production/destruction of each species i by reaction k can be simply evaluated as

$$\hat{\omega}_{i,k} = (v''_{i,k} - v'_{i,k}) \omega'_k$$

To evaluate the overall production/destruction rate of species i , we add the rates from each reaction k .

$$\hat{\omega}_i = \sum_{k=1}^N \hat{\omega}_{i,k}$$

The result is the net production or destruction rate for each species i ($\hat{\omega}_i$) in molar basis.

This can be converted to the mass-based rate of production/destruction for each species that appears in the species conservation equations

$$\dot{w}_i = MW_i \hat{\omega}_i.$$

3. COMPUTATIONAL PROCEDURES

This section presents the computational scheme that was used to calculate the equilibrium Rankine–Hugoniot curves and the transient ZND detonation structure. For a successful numerical solution of the steady state ZND detonation, careful attention must be paid to the stiffness of the ordinary differential equations for chemically reacting flow and the numerical scheme that is used for their computation.

Cantera Chemically Reacting Flow Program

Cantera is a collection of object-oriented software tools for solving problems involving chemical kinetics, thermodynamics, and transport processes. The code was developed at Caltech by David Goodwin [15] during the last decade and is maintained as an open-source project. In order to carry out a reacting flow simulation using Cantera, a proper chemical reaction mechanism is required. The Gas Research Institute Mechanism version 3.0 (GRI-3.0) has been developed for methane and natural gas oxidation, and has been exhaustively tested against a wide range of experimental data [16]. It is a compilation of 325 elementary chemical reactions and the associated rate coefficient expressions and thermochemical parameters for the 53 species involved in those reactions. GRI-3.0 has been optimized for hydrogen, methane, and natural gas fuels.

Computational Algorithm

Cantera simultaneously handles equations of state and thermodynamic properties through its thermodynamic manager, chemical kinetics through its chemical manager, and transport coefficients and processes through its transport manager. It uses all three managers to calculate the macroscopic behavior of chemically reacting flow.

The thermodynamic manager applies the thermal and caloric equations of state to calculate the thermodynamic properties of an ideal gas reacting mixture

$$P = \rho \bar{R} T \frac{1}{\sum_i X_i MW_i}$$

where \bar{R} is the universal gas constant, X_i represents the mole fractions of each species i , and MW_i is the molecular weight of each species i .

The heat capacity, sensible enthalpy, and standard entropy at the temperature can be calculated by the NASA polynomial parameterizations [15] of the caloric equation of state for ideal gases, which are written as follows

$$\begin{aligned} \frac{C_{p,i}(T)}{\bar{R}} &= a_0 + a_1 T + a_2 T^2 + a_3 T^3 + a_4 T^4 \\ \frac{h_i(T)}{\bar{R}T} &= a_0 + \frac{a_1}{2} T + \frac{a_2}{3} T^2 + \frac{a_3}{4} T^3 + \frac{a_4}{5} T^4 + a_5 \\ \frac{s_i^0(T)}{\bar{R}} &= a_0 \ln(T) + a_1 T + \frac{a_2}{2} T^2 + \frac{a_3}{3} T^3 + \frac{a_4}{4} T^4 + a_6 \end{aligned}$$

All coefficients ($a_0 - a_6$) of NASA polynomials are tabulated as a Cantera input file (cti file).

The chemical kinetics manager computes the reaction rates of progress, equilibrium constants, and species creation and destruction rates for each species i . A Cantera input file also contains reaction entries for each reaction in the chemical mechanism. The chemical manager uses this information to form the source terms (production/destruction rates) that appear in the species conservation equations as shown in the previous section. For example, when a reaction in the chemical mechanism follows the simple Arrhenius form, the Cantera chemical manager tabulates the pre-exponential coefficient, the temperature exponent, and activation energy for each reaction k (A_k, n_k, E_k).

The transport manager handles the gas-phase transport properties such as viscosity, thermal conductivity, and binary or multi-component diffusion coefficients. During the present work the inviscid Euler equations are computed, therefore the transport manager is not utilized.

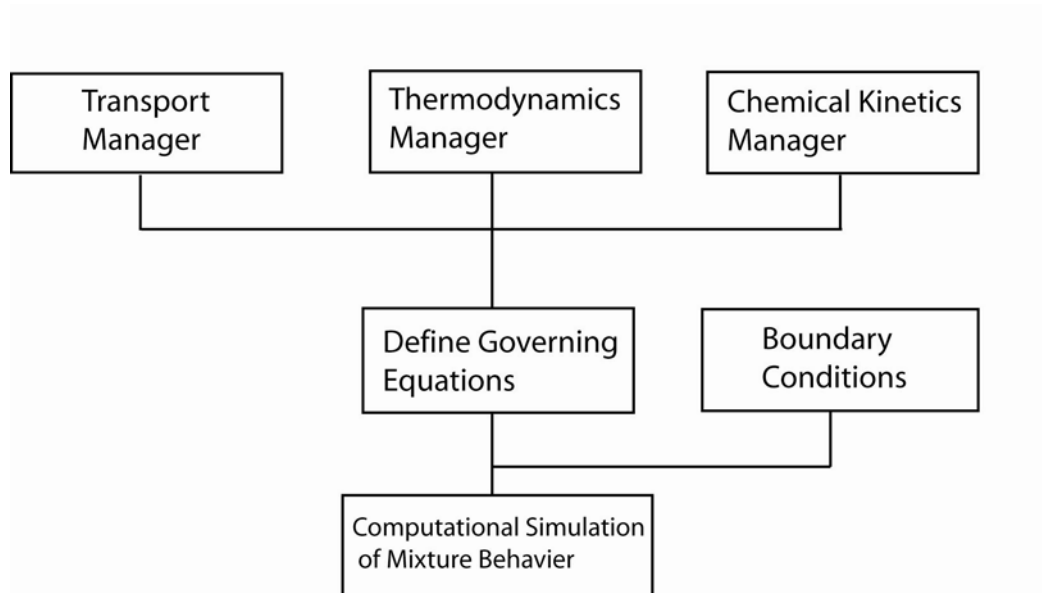


Figure 3.1. Schematic diagram of computing chemically reacting flow by *Cantera*

As seen in Figure 3.1, the Cantera code uses all three aforementioned managers in combination with appropriate solvers to calculate reacting flows of specific dimensionality and complexity, such as transient zero dimensional (0D) open and closed well-stirred reactors, steady state 1D propagating flames, 1D opposed jet flames, etc. As will be shown subsequently, the 0D solvers can be used for the transient ZND calculation, but their use is highly problematic. The present work used the thermodynamic and chemical managers of Cantera with an externally set up 1D solver to calculate the spatial variation of the ZND detonation.

Rankine-Hugoniot Analysis

The solution of the equilibrium endpoints of a detonation *cannot* involve *any* knowledge of the structure of the detonation wave. Considering steady, planar, and 1D detonation waves, the equilibrium state solution of the integral conservation laws presented in the previous section only requires thermodynamic calculations; this approach is the Rankine-Hugoniot analysis [17].

When the velocity of the final state (1) is eliminated from the mass and momentum conservation equations, the results define a line in the pressure-specific volume (P - v) diagram, i.e. the Rayleigh line, which is expressed by the following equation

$$\frac{P_1 - P_0}{v_1 - v_0} = -\frac{u_0^2}{v_0^2} = -(\rho_0 u_0)^2 = -(\text{mass flux})^2$$

where v is the specific volume (reciprocal density). An infinite number of Rayleigh lines can pass from one initial point (P_0, v_0) , corresponding to different detonation velocities (u_0) and mass fluxes $(\rho_0 u_0)$. The limiting cases of Rayleigh lines are the horizontal ($u_0 = 0$) and the vertical ($u_0 = \infty$). The vertical Rayleigh line represents the constant volume detonation in which all material reacts instantaneously while the horizontal one is a constant-pressure process.

The Hugoniot curve in the P - v diagram is obtained by eliminating the upstream and downstream velocities from the energy equation by using the mass and momentum equations to obtain

$$h_1 - h_0 = \frac{1}{2}(P_1 - P_0)(v_1 + v_0)$$

or

$$C_p (T_1 - T_0) - \frac{1}{2}(P_1 - P_0)(v_1 + v_0) = Q$$

where C_p is the average constant specific heat, and Q is heat generation through the reaction. Since the velocity is eliminated, the Hugoniot curve expresses a relationship solely among thermodynamic properties.

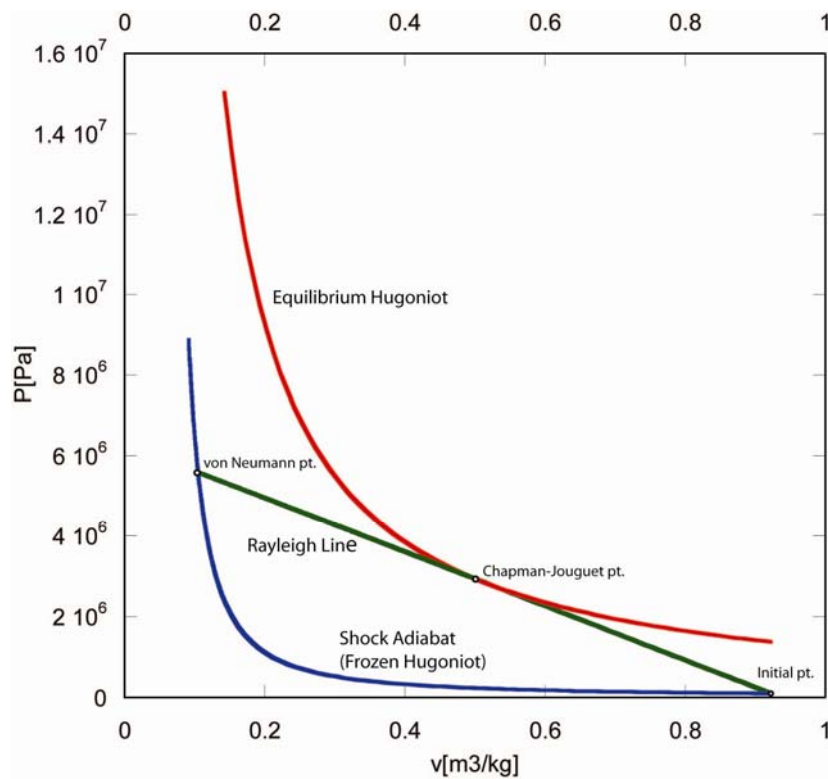


Figure 3.2. Rayleigh line and Hugoniot curves for Chapman-Jouguet methane/oxygen detonation

Figure 3.2 shows the Rayleigh line and two Hugoniot curves (frozen and equilibrium) for stoichiometric methane-oxygen detonation [18]. The location of the two Hugoniot curves is specified by the value of heat generation through the reaction. A frozen

Hugoniot curve is the collection of all possible thermodynamic states without any reaction ($Q = 0$). Inviscid shock compression does not change the mixture composition, therefore a frozen Hugoniot curve indicates all of the possible post-shock thermodynamic states of an adiabatic compression, hence the usual title ‘shock adiabat.’ An equilibrium Hugoniot curve is the collection of all possible thermodynamic states after the reactants have fully reacted and equilibrium has been achieved in the products. The equilibrium Hugoniot shown in Figure 3.2 was calculated using the Cantera thermodynamic manager, so no assumption of $C_p = \text{constant}$ is necessary.

The thermodynamic state after the inviscid shock must satisfy both Rayleigh line and shock adiabat conditions. This unique intersection of the two curves is the von Neumann point (VNP), and it denotes the post-shock thermodynamic state.

Similarly, the conservation equations require that the final equilibrium state lies on both the Rayleigh line and the equilibrium Hugoniot curves. For a sufficiently small mass flux through the 1D system, the Rayleigh line and Hugoniot curve have no intersection, so there is no solution that satisfies the equilibrium condition. But there exists a minimum detonation velocity (Chapman-Jouguet or CJ velocity), which is the point where the Rayleigh line is tangent to the equilibrium Hugoniot. It can be shown that the flow is sonic at this point [14].

Discontinuous Shock Calculation

Given the initial detonation velocity and thermodynamic properties, we need to calculate the post-shock conditions at the VNP. A dedicated Cantera shock and detonation tool box was developed at Caltech by Joseph Shepherd [18, 19, 20, 21]. The toolbox uses a Newton-Raphson scheme to solve the algebraic equations that connect the equilibrium conditions. The scheme is used here to solve for the jump conditions of a Chapman-Jouguet detonation. Recall the momentum and energy equations at jump conditions as

$$P = (p_1 + \rho_1 u_1^2) - (p_0 + \rho_0 u_0^2)$$

$$H = \left(h_1 + \frac{1}{2} u_1^2 \right) - \left(h_0 + \frac{1}{2} u_0^2 \right)$$

The exact solution to the discontinuous jump occurs when both H and P are identically zero. An approximate solution can be obtained by simultaneously iterating these two equations until H and P are less than a specified tolerance. An iteration algorithm can be developed by making an initial guess for the values of temperature and specific volume of the downstream thermodynamic state 1, and iterate until a solution has been obtained. The shock and detonation toolbox has been extensively used in this study.

Well-stirred Reactor (WSR)

In the early phases of the present work, the ZND detonation was simulated by using the built-in Cantera module of a Well-Stirred Reactor (WSR). The WSR is an idealization that assumes that all chemical reactions occur homogeneously in space, and the extent of product formation is governed simply by the thermochemistry of the reactor, as well as by the residence time. Once inside the reactor, the gases are presumed to mix instantaneously and perfectly with the gases already resident in the reactor. In reality, mixing cannot be perfectly instantaneous. In practice, the well-stirred reactors are designed to create intense turbulence that enhances mixing [22].

The benefit of using the WSR model for the ZND detonation calculation is that the reaction zone can be simulated in time; therefore, this simulation can generate the transient states of a ZND detonation. The WSR contains reactants at the post-shock (VNP) state, i.e. the initial state before the ZND reaction. The WSR is separated by a reservoir that contains the final equilibrium (CJ) states of the mixture with a freely

moving piston. When the WSR is a closed system, the mass is constant, while the volume can be changed, resulting in thermochemistry changes. Figure 3.3 shows the set-up of the well-stirred reactor system used for ZND reaction zone calculation.

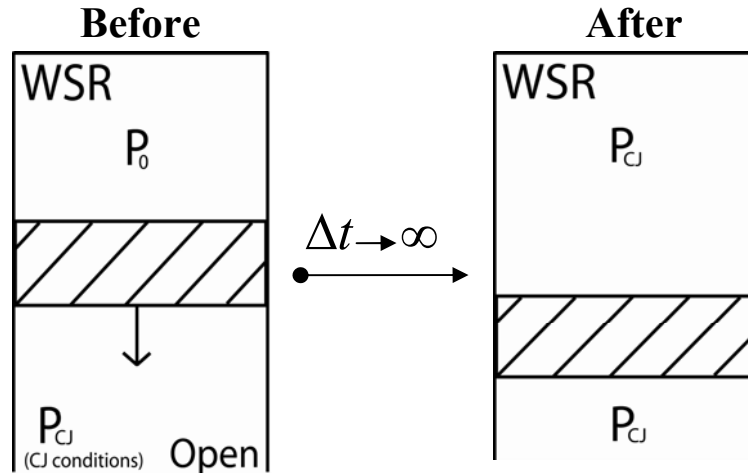


Figure 3.3. A Well-Stirred Reactor (WSR) model for the computation of a ZND reaction zone

As the reaction progresses inside the WSR, the reacting mixture pushes the piston until the pressure within the WSR reaches the pressure of the reservoir outside. Therefore, the final pressure of the mixture will be the Chapman-Jouguet pressure. Assuming that there will be full conversion to products at the end of the WSR reaction, and since the system is adiabatic, the final equilibrium temperature in the WSR is going to be equal to the equilibrium adiabatic flame temperature. As the pressure has already been set to that of the CJ point, the equilibrium state of the WSR is identical to the CJ state since they share pressure, temperature, and composition.

Figure 3.4 shows the results of WSR simulation using three different piston areas. When the piston area is small, the combustion inside a WSR occurs faster than the expansion

(Case 1 in Figure 3.4). This case is similar to the constant-volume combustion, and most mixture expansion occurs after the combustion has been completed. In fact, the transient pressure exceeds the von Neumann value, which is the theoretical maximum pressure encountered on a ZND detonation. With a moderate piston area the combustion and expansion rates are similar (Case 2 in Figure 3.5). When a piston area is large, expansion occurs faster than combustion (Case 3 in Figure 3.6). The mixture pressure immediately decreases to the Chapman-Jouguet pressure, and combustion takes place after the expansion. Thus, this case is similar to a constant-pressure combustion process taking place at the Chapman-Jouguet pressure.

At first glance, the WSR seems like a good model for analyzing a transient state of ZND detonation; however, the WSR poses a significant problem. As seen in Figure 3.4, either the piston area or the piston velocity must be specified in time in such a way that the ZND detonation will proceed along the Rayleigh line. This implies that we need to know the change of all physical properties before running the simulation. Thus, a WSR is not an adequate model for the simulation of the reaction zone of ZND detonation.

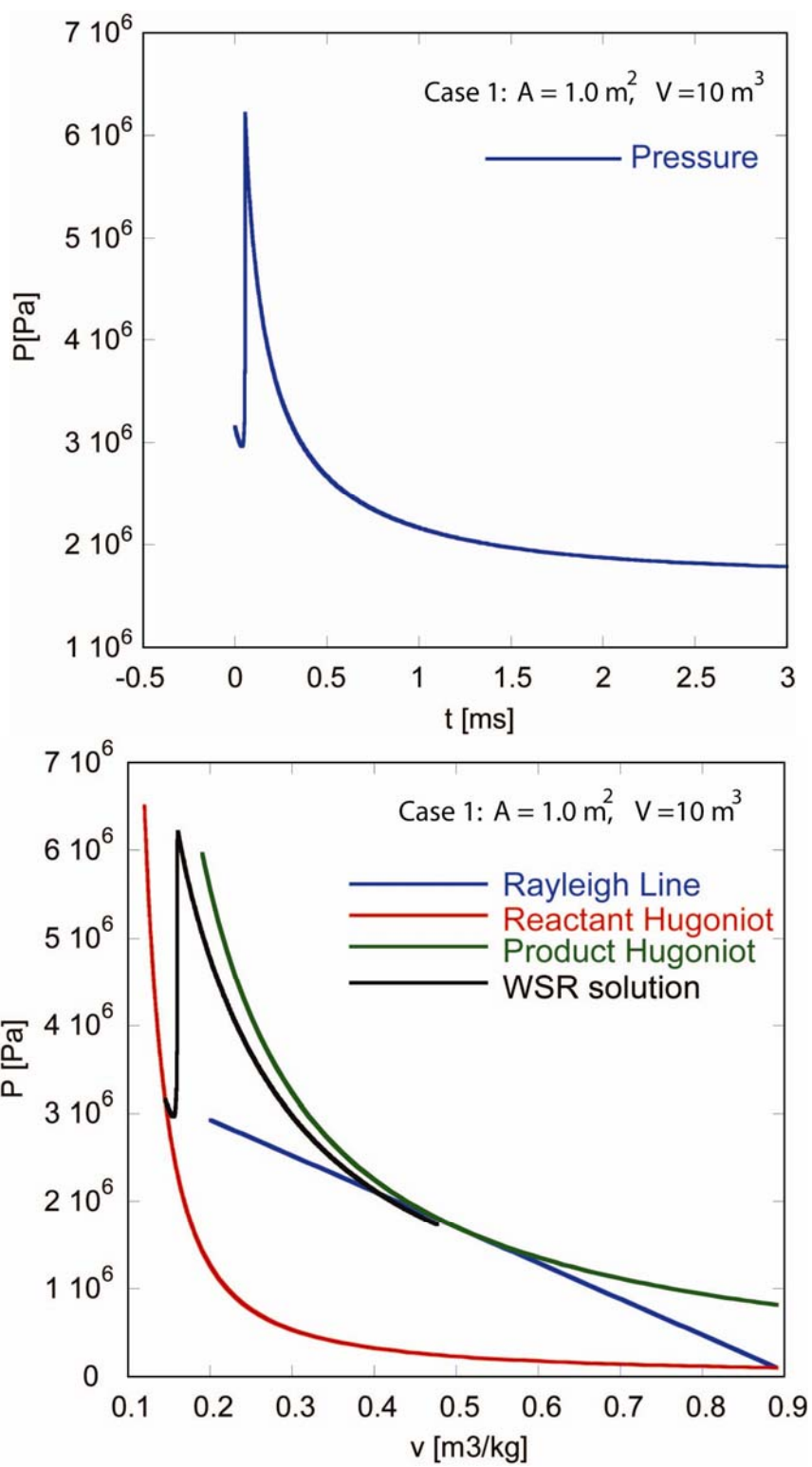


Figure 3.4 Results of well-stirred reactor model for $A = 1.0 \text{ m}^2$

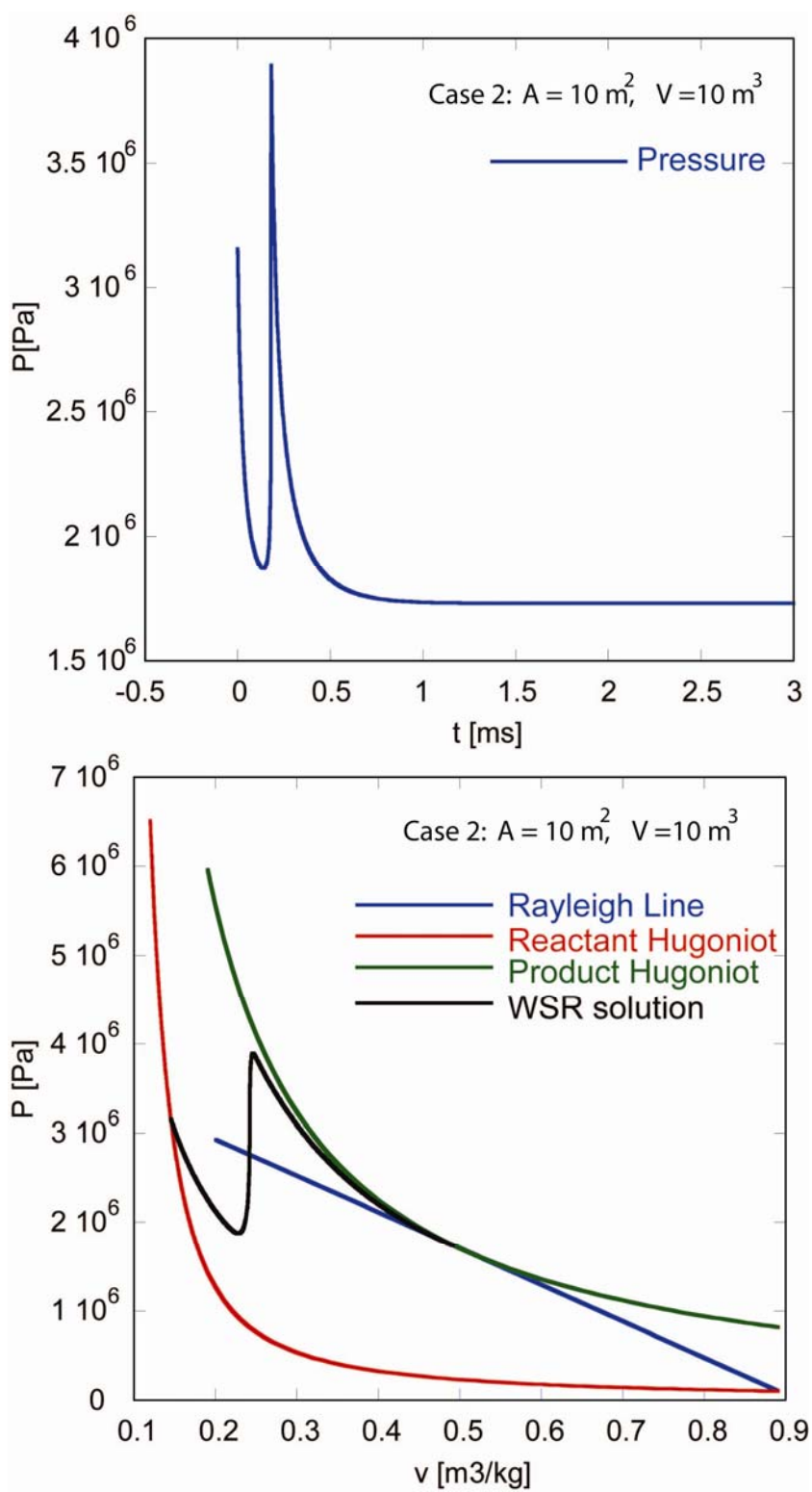


Figure 3.5 Results of well-stirred reactor model for $A = 10 \text{ m}^2$

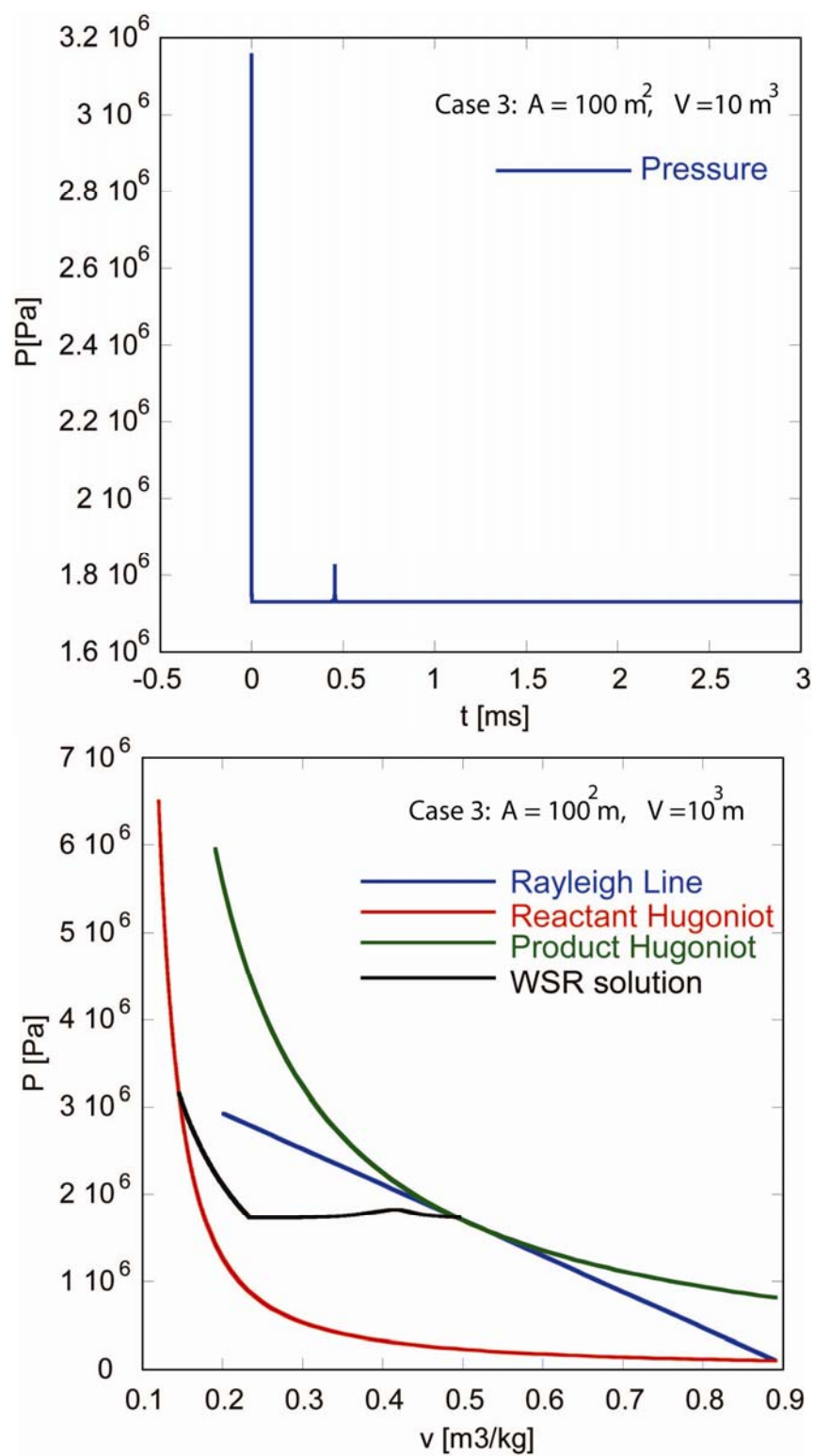


Figure 3.6 Results of well-stirred reactor model for $A = 100 \text{ m}^2$

4. NUMERICAL METHODOLOGY AND STABILITY ANALYSIS

Numerical Methodology

The ZND reaction zone is calculated using both explicit and implicit schemes. An explicit algebraic solution for the mass, momentum, and energy conservation equations computes velocity, pressure, and enthalpy of the reacting flow in each step using the conservation equations

$$\begin{aligned}\rho u &= \text{const} \\ p + \rho u^2 &= \text{const} \\ h + \frac{1}{2}u^2 &= \text{const}\end{aligned}$$

The species conservation equations are solved using an implicit third-order Backward Differential Formula (BDF) method. The code was written in-house, and is based on an existing variable-coefficient ODE solver (VODE) for stiff and non-stiff problems [23]. The species equations are written below, and \dot{w}_i is the chemical source term to be calculated by the Cantera chemical manager for every single step.

$$\frac{dY_i}{dx} = \frac{\dot{w}_i}{\rho u}$$

For stiff problems, the accuracy of the BDF method can be selected *a priori* to correspond to orders between first and fifth. However, the stability of the BDF method decreases for numerical schemes that are more than fourth-order accurate [24], and orders above sixth result in unstable schemes. The present computations use a third order BDF scheme.

The Cantera thermodynamic manager calculates all thermodynamic properties at each step using a constant pressure and enthalpy formulation for the open system, while the Cantera chemical manager calculates the species destruction/production rates needed in the right hand side of the species conservation equations. Then, the BDF scheme updates the values of composition (Y_i) and new velocity, pressure, and enthalpy (u, P, h) are computed algebraically. Thermodynamic variables and species mass fractions change in each step within the reaction zone. Therefore, it is difficult to compute the reactive source terms and the thermodynamic properties using a fully implicit method, solely because the Cantera managers must compute the thermodynamic variables and chemical sources explicitly in every step of the computation. Hence the mass production/destruction rates cannot be calculated implicitly, i.e. for many different steps at the same time, even if the actual integration is carried out by the BDF implicit scheme. The scheme used in this study separately solves the species equations and the mass, momentum, and energy equations in every step on the reaction zone.

Limits on Step-size

In order to provide examples of the numerical scheme and assess its accuracy and convergence properties, a number of computations were repeated using different step sizes. Figure 4.1 shows the solution of a stoichiometric CJ methane/oxygen ($\text{CH}_4\text{-O}_2$) detonation using six different step-sizes ($\Delta x = 10^{-7}, 5 \times 10^{-8}, 10^{-8}, 5 \times 10^{-9}, 10^{-9}, 5 \times 10^{-10}$, all in meters).

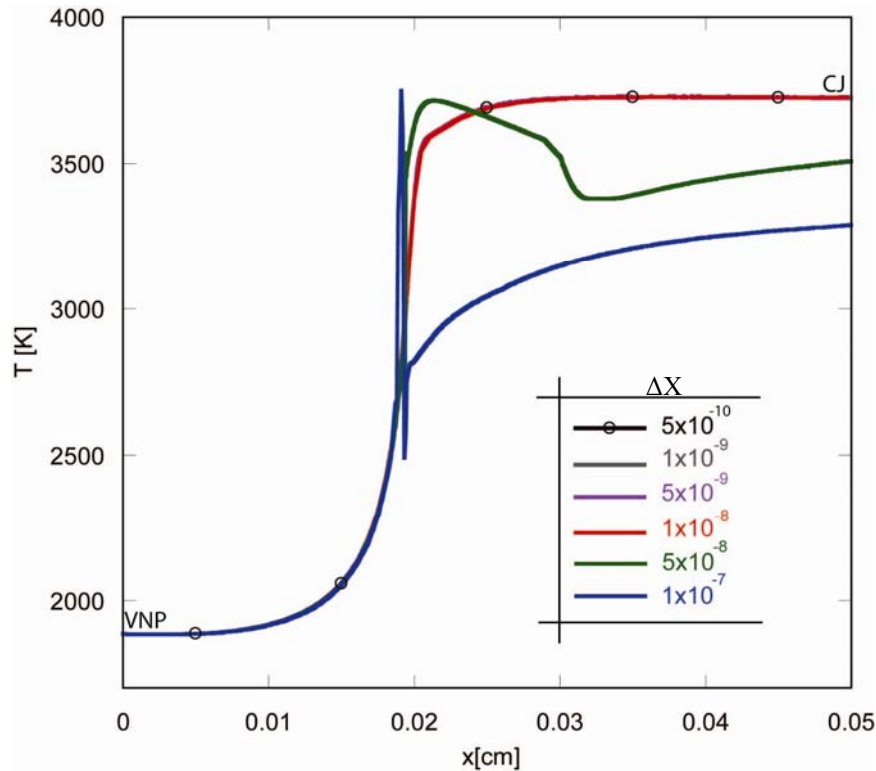


Figure 4.1. Temperature profiles of the $\text{CH}_4\text{-O}_2$ Chapman-Jouguet (CJ) detonation using different step-sizes

The circles plotted on the graph point to a converged solution, i.e. number of different computations that collapse onto a single curve. For a sufficiently small step-size (less than 10^{-8} m), the equilibrium temperature converges to the CJ condition, while for coarser step sizes (above 5×10^{-8} m) the temperature profile shows unphysical oscillations and the final equilibrium temperature is lower than the CJ one.

Methane is completely consumed during the ZND reaction, no matter what step-size is set in the simulation (Figure 4.2). A cursory look at the O_2 profiles shows the same effect of reactants approaching zero at the CJ point. However, the temperature resulting from setting a larger step-size is lower than the CJ condition; thus, we need to examine other, minor species which may cause the lower equilibrium temperature.

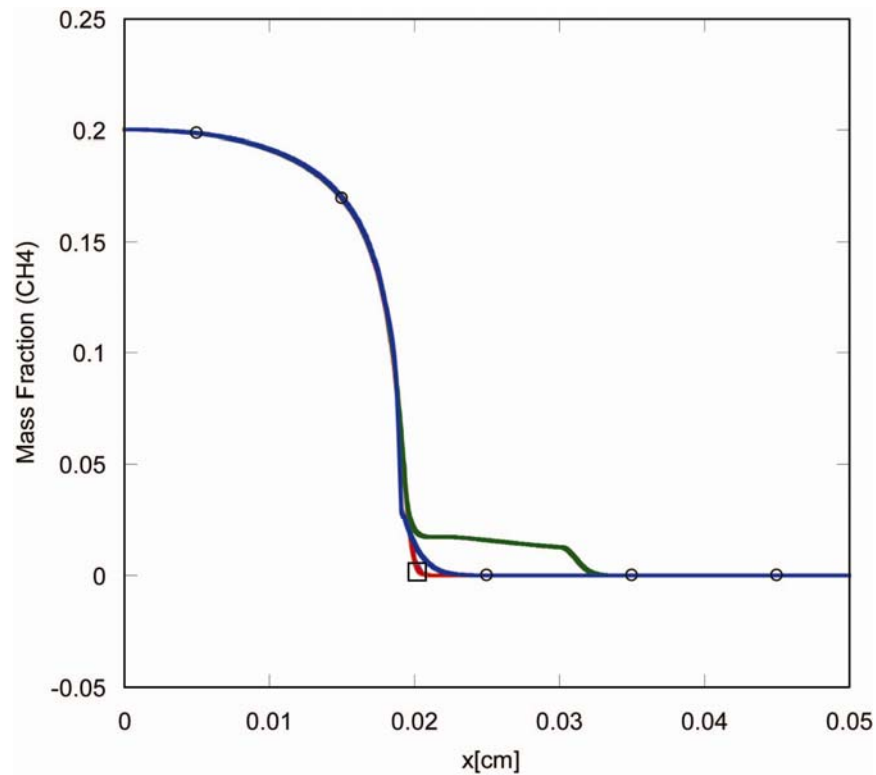


Figure 4.2. Mass fraction of methane molecules by using different step-sizes, legend as in Figure 4.1

During the parametric computations, it was found that a smaller step-size yields a more accurate value. Figure 4.3 is a magnification of the square region shown in Figure 4.2. As is evident from the expanded figure, convergence is little improved by drastic reduction of the step size below 10^{-8} m.

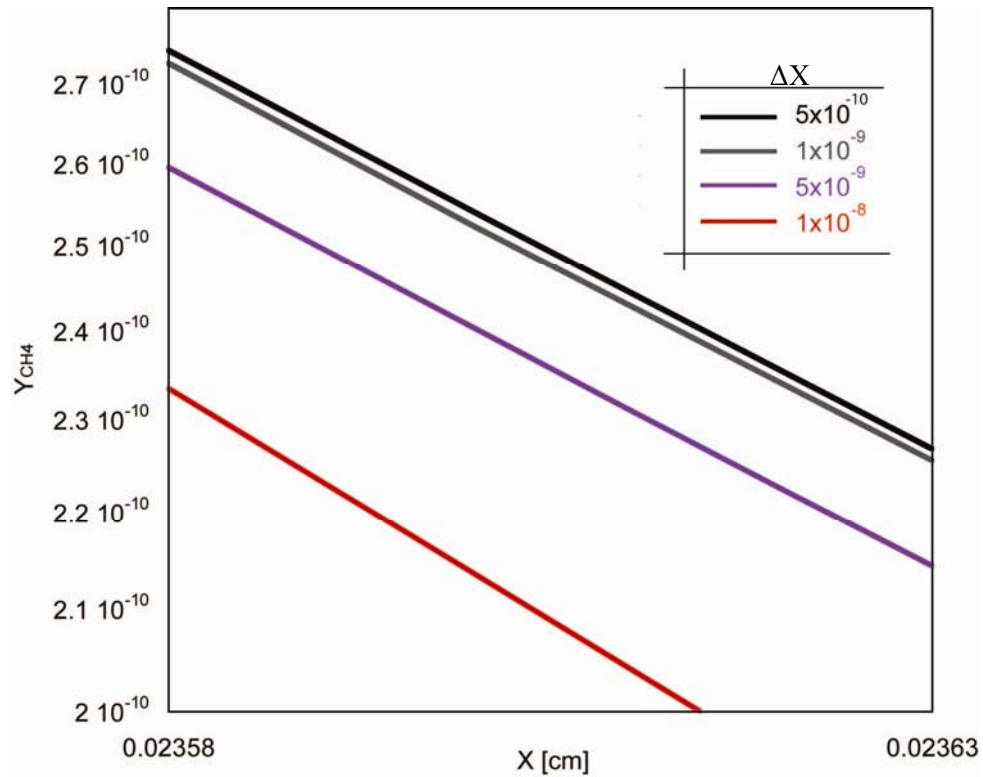


Figure 4.3. Detail from Figure 4.2

For the study of a chemically reacting flow, the system of ordinary differential equations (ODEs) is a stiff system with a wide range of time/length scales [25]. For a methane/oxygen ($\text{CH}_4\text{-O}_2$) ZND detonation, the characteristic time/length of a free radical species, such as a hydrogen atom, is extremely short, while the characteristic time/length of CH_4 molecules is long. This time/length-scale difference leads to rapid changes in the solution of the fast species, and the numerical algorithm must resolve that large dynamic range of scales. When the step-size is large, substantial equilibrium values of H and O radical concentrations appear during the simulation (Figures 4.4 and 4.5) which should not happen in a realistic situation, as these species are highly reactive. The high values of energetic radicals, such as H, lead to artificial temperature increases early in the computation (e.g. $x = 0.02$ cm of Figure 4.1).

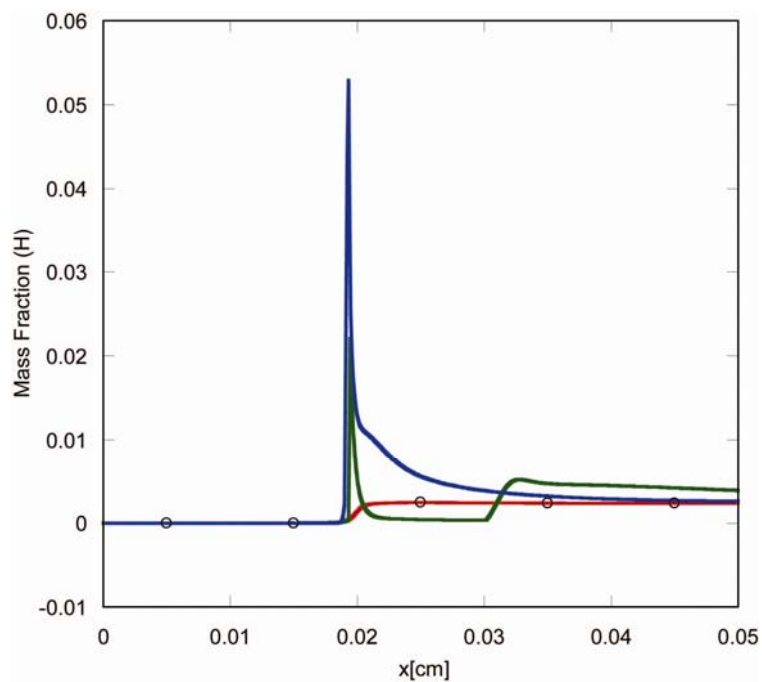


Figure 4.4. Mass fraction of hydrogen radicals using different step-sizes, legend as in Figure 4.1

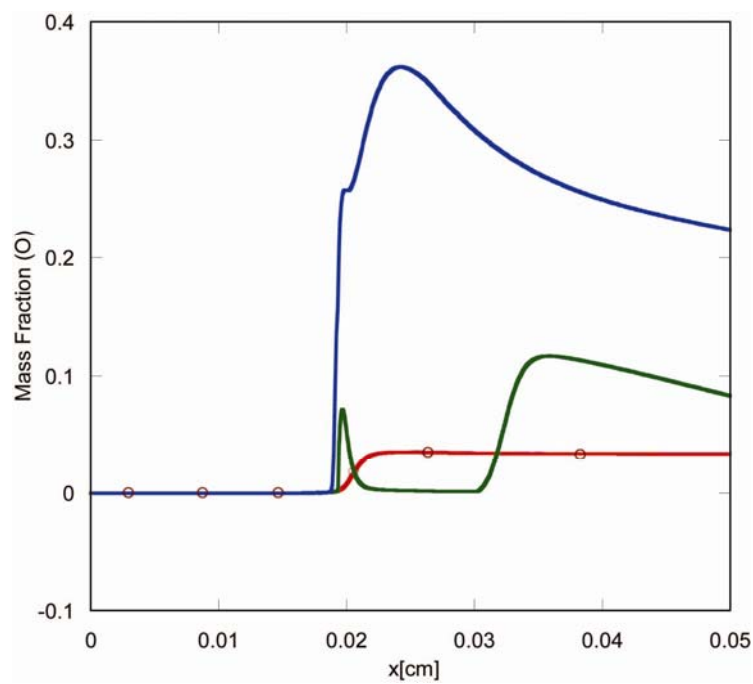


Figure 4.5. Mass fraction of oxygen radicals using different step-sizes, legend as in Figure 4.1

The first peak of the H radicals is correlated to the temperature oscillation for coarse step-sizes (10^{-7} m). When the step size is 5×10^{-8} m, the H and O show a second peak at $x \simeq 0.03$ cm, at which point the remaining methane is consumed. Thus, there are two occurrences of combustion that take place when the step-size is relatively large. For final step-sizes (less than 10^{-8} m) the profiles of the H and O radicals successfully converge, and so does the temperature profile. It should be noted that due to the high equilibrium temperature some dissociation takes place, leading to small values of H, O, and other radical species at equilibrium.

A similar issue can be identified with all other fast-lived radical species. The stiffness of the equations leads to problems whenever the species that have very short characteristic times exhibit sufficiently high reaction rates. When the step-size is large, the mass fractions of CH radicals are also amplified and result in a sharp maximum (see Figure 4.6). The degree of CH radical amplification is proportional to the step-size. Even though the CH radicals are not present at equilibrium, their transient behavior is similar to that of the O and H radicals.

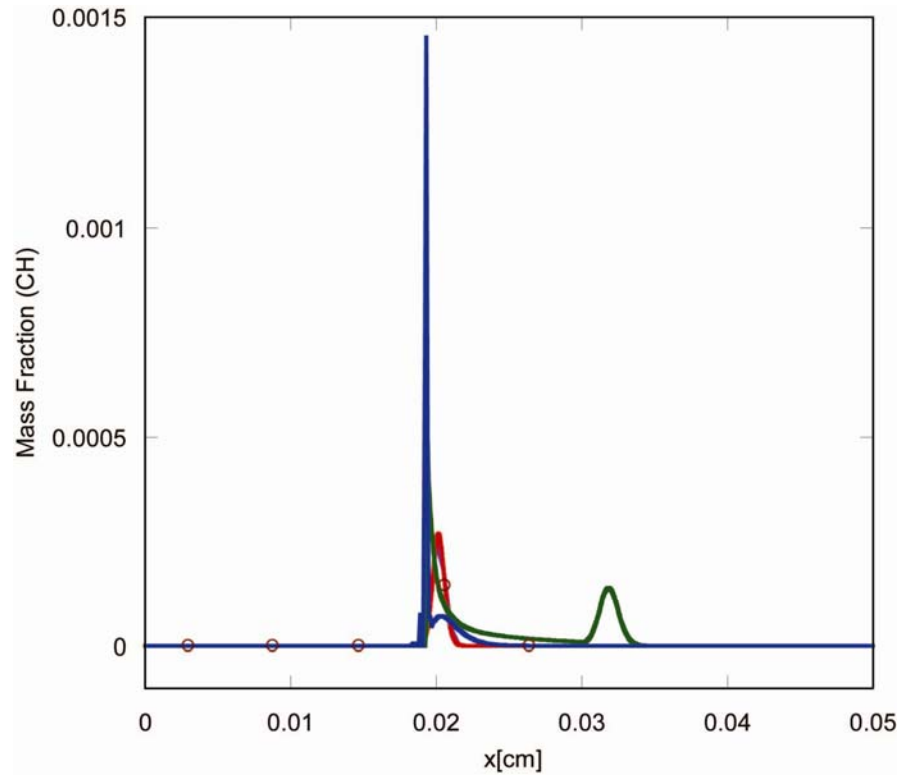


Figure 4.6. Mass fraction of CH radicals using different step-sizes, legend as in Figure 4.1

Thus, we can conclude from the convergence test of the species equations that for successful implicit integration the step-size needs to be less than approximately 10^{-8} m. When the step-size is not sufficiently small, the third-order BDF method does not yield the appropriate mass fractions of the minor species and does not converge to a physical solution. If there are substantial concentrations of species such as H and O present at equilibrium, the temperature will be lower than the theoretical CJ value. The numerical solution accumulates errors, and the errors will continue to amplify until the method ‘blows up’ [25].

Explicit Versus Implicit Methods and Their Orders

Since the species equations involve highly non-linear source terms, their analytic solutions are usually very hard to obtain. For the study of explicit and implicit ODE accuracy, the example of an easily solvable system of linear stiff ordinary equations is given below.

$$\begin{aligned}y_1' &= 2000y_1 - 999.75y_2 + 1000.25 \\y_2' &= y_1 - y_2\end{aligned}$$

These equations will be solved using both explicit and implicit methods to determine which is more accurate. The initial condition is set as $[y_1, y_2] = [0, -2]$, and the step-size is 10^{-4} m. The analytical solution of the system of stiff ODEs can be found as

$$\begin{aligned}y_1(x) &= -1.499875e^{(-0.5x)} + 0.499875e^{(-2000.5x)} + 1 \\y_2(x) &= -2.999975e^{(-0.5x)} - 0.000015e^{(-2000.5x)} + 1\end{aligned}$$

The characteristic scales of the first and second terms differ by four orders of magnitude, with the second term decaying very fast, and the first decaying slowly.

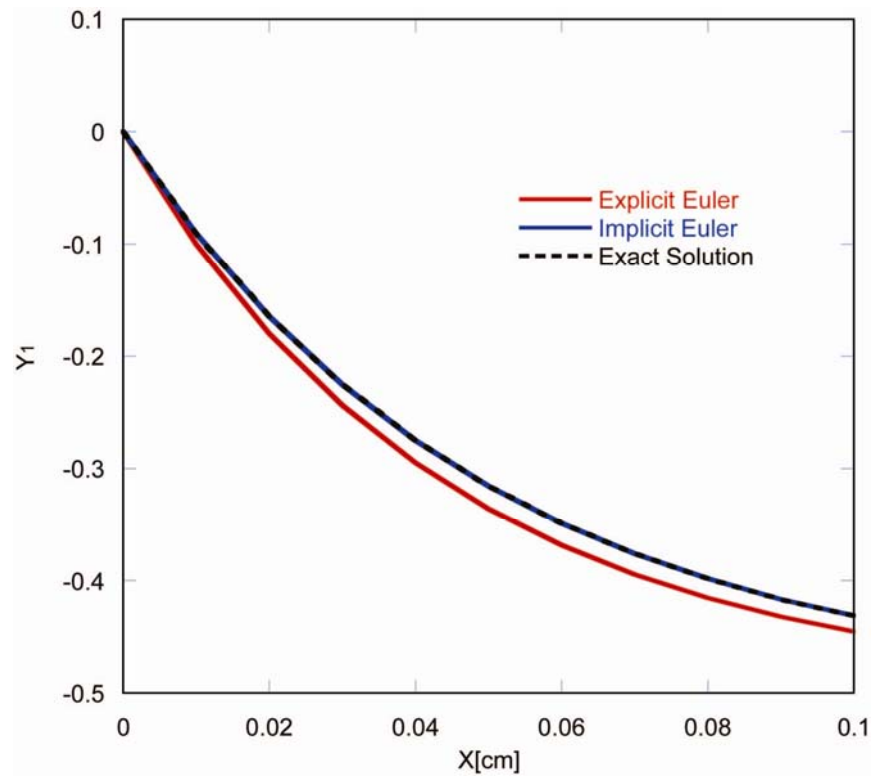


Figure 4.7. Exposition of the implicit Backward Differential Formula (BDF) scheme

Figure 4.7 shows the solution $y_1(x)$ for three different cases: an explicit first-order Euler integration, an implicit third-order BDF, and the exact solution (practically identical to the analytic one). The explicit first-order Euler integration method is clearly less accurate than the implicit method because, for large step sizes, instability is present in the explicit method.

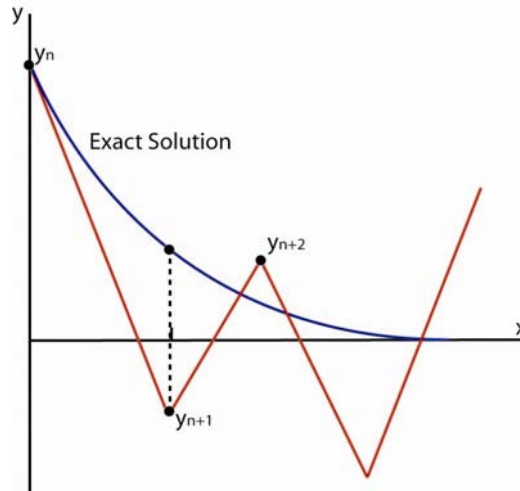


Figure 4.8. Qualitative description of a stiff Ordinary Differential Equation problem

A qualitative explanation of the numerical instability present in explicit numerical schemes is shown in Figure 4.8. There the dependent variables (y_1 or y_2) are supposed to be known at some point (y_n), along with the slope (y'_n). When the step-size is very large, despite the fact that we know both the value y_n and the slope exactly, we grossly under-predict the value of y_{n+1} . An explicit method uses the erroneous value of y_{n+1} to calculate the following point in the solution (y_{n+2}) that amplifies the error of the solution. When the step-size is too large, an explicit Euler integration cannot converge to the right solution. In the example problem presented here, the step-size is relatively small (10^{-4} m), and an explicit method converges to a solution which is acceptable and comparable to the exact solution, yet still different from it by the error accumulated during the integration [25].

A large solution error (10^{-4}) appears in each time step of an explicit Euler method as shown in Figure 4.9. The solution yielded by the implicit third-order BDF is very close to the exact solution. The error of the technique is on the order of 10^{-12} and the technique is stable even for relatively large time steps (10^{-4} m). This feature ensures that this method is stable for a sufficiently small time step.

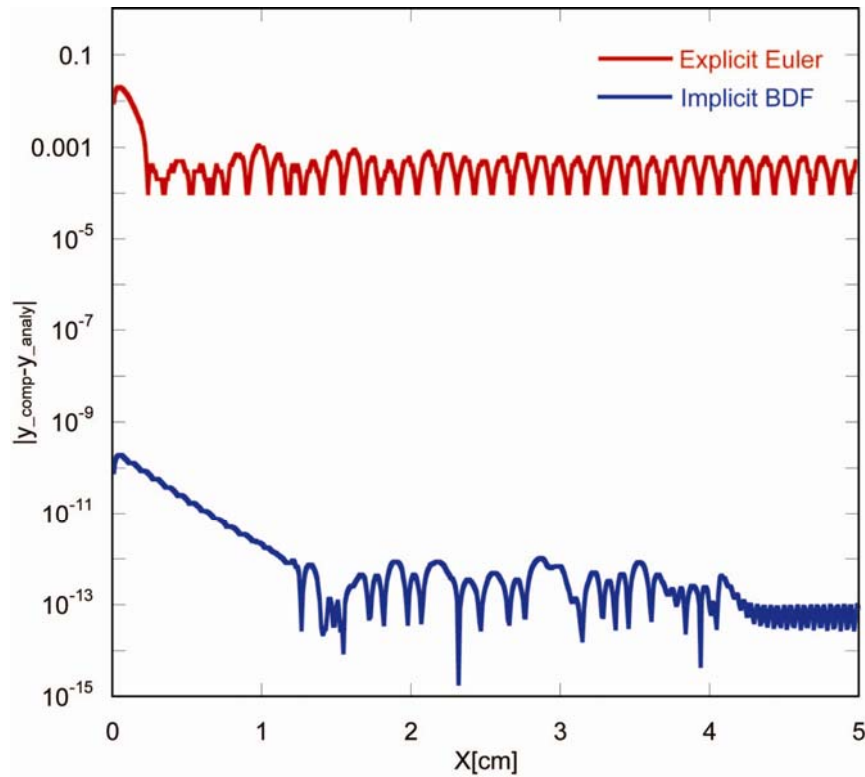


Figure 4.9. Errors between explicit Euler and implicit Backward Differential ODEs solutions

The truncation errors of a first-order forward Euler method and a third-order backward differential method are as follows [26]:

$$\text{1st order Explicit Euler method: } -\frac{1}{2} \frac{\partial^2 y}{\partial x^2} (\Delta x)$$

$$\text{3rd order Implicit BDF method: } -\frac{1}{4} \frac{\partial^4 y}{\partial x^4} (\Delta x)^3$$

When the step-size is $\Delta x \sim 10^{-4}$ m, the truncation error of the first-order explicit Euler method is of the same order as the step-size (10^{-4} m), while the error of the third-order BDF method is on the order of 10^{-12} . Both truncation errors are clearly correlated to the solution errors shown in Figure 4.9. For stiff differential equations, the first-order explicit method is not optimal because it will propagate the errors along with the

solution, such that at the final equilibrium point, the error can be significant. The third-order implicit method is a better approximation to the desired solution, since it resolves the stability problems associated with stiffness. However, because it is a higher-order implicit method, more computational time is required at each step to solve the system of nonlinear species equations.

Required Computational Time Study

As already discussed, to avoid numerical instabilities, the step-size needs to be sufficiently small so that numerical round-off errors are damped and not amplified, and the solution of the ODEs is accurate. The elapsed computational time linearly increases as the step-size decreases (Figure 4.10).

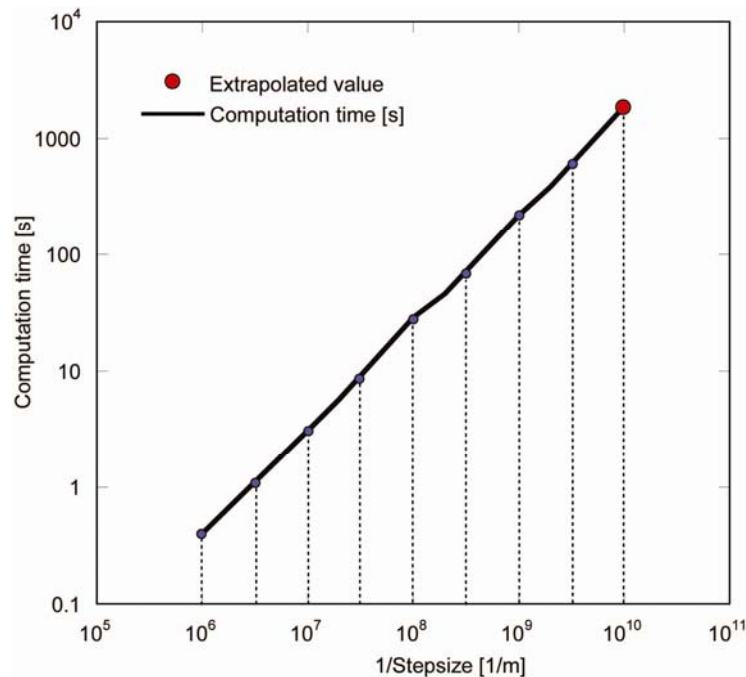


Figure 4.10. Total computational time for different step-sizes

For step-size of 10^{-10} m the extrapolated computational time is approximately 32 minutes (red point). This is not a prohibitive computational time, yet computations with such fine step-sizes routinely fail due to lack of memory. No attempt was made to improve the memory allocation scheme in the present study, as the coarser step-sizes (e.g. 10^{-8} m) exhibited good convergence.

5. RESULTS AND ANALYSIS

H₂-O₂ Reaction Mechanism

Hydrogen oxidation is a relatively simple and well-understood phenomenon, both theoretically and experimentally. The hydrogen/oxygen reaction mechanism will be briefly reviewed here, since it is applicable to the ZND detonation of hydrogen fuel; this mechanism is also interesting as a subset of all hydrocarbon fuel oxidation mechanisms. Table 5.1 shows some of the reactions that can occur in hydrogen/oxygen reaction systems. The most probable initiation step at low temperatures is the generation of relatively stable hydroperoxyl (HO₂) radicals and highly reactive hydrogen (H) radicals (RXN 1) by the hydrogen and oxygen molecules. At very high temperatures, the hydrogen and oxygen molecules directly dissociate to hydrogen and oxygen radicals (RXN 2, 3).

When the mixture (in the von Neumann state) is at a sufficiently high temperature ($T > 1200\text{K}$), the initiation step provides hydrogen radicals. These hydrogen radicals initiate the chain branching mechanism (RXN 4-7), from which hydroxyl (OH), oxygen, and more hydrogen radicals are produced. These reactions are the primary means by which the OH concentration becomes significant and can play a role in the reaction processes. These reactions release significant amounts of energy, which accelerates the explosion. Note that the concentration of H radicals is replenished through this process, therefore, there is no chemical barrier to prevent the system from becoming explosive.

Most of the chemical energy is released through the final oxidation process (RXN 8-12), i.e. the termination process. During the termination process, the accumulated radicals exothermically react to generate water (H₂O) molecules. RXN 10 is technically a propagation process, but the HO₂ radical is relatively un-reactive. The hydroxyl molecule dominates the final oxidation process in the hydrogen/oxygen reaction (RXN

11, 12). Therefore, the rate of hydroxyl generation is important for determining the explosion limits of hydrogen/oxygen combustion.

Table 5.1. Possible reaction mechanism of H₂-O₂

RXN 1: H ₂ + O ₂ ↔ HO ₂ + H	(Initiation)
RXN 2: H ₂ + M ↔ 2H + M	(Initiation)
RXN 3: O ₂ + M ↔ 2O + M	(Initiation)
RXN 4: H + O ₂ ↔ O + OH	(branching)
RXN 5: O + H ₂ ↔ H + OH	(branching)
RXN 6: H ₂ + OH ↔ H ₂ O + H	(propagation)
RXN 7: O + H ₂ O ↔ OH + OH	(branching)
RXN 8: H + O + M ↔ OH + M	(termination)
RXN 9: HO ₂ + H ↔ H ₂ O + OH	(termination)
RXN10: H + O ₂ + M ↔ HO ₂ + M	(propagation)
RXN11: OH + HO ₂ ↔ H ₂ O + O ₂	(termination)
RXN12: OH + H + M ↔ H ₂ O + M	(termination)
RXN13: HO ₂ + H ₂ ↔ H ₂ O ₂ + H	(propagation)
RXN14: H ₂ O ₂ + M ↔ 2OH + M	(branching)
RXN15: HO ₂ + HO ₂ ↔ H ₂ O ₂ + O ₂	(termination)
RXN16: HO ₂ + H ↔ 2OH	(propagation)
RXN17: HO ₂ + O ↔ OH + O ₂	(propagation)
RXN18: H + H + M ↔ H ₂ + M	(termination)
RXN19: O + O ↔ O ₂ + M	(termination)
RXN20: H + O + M ↔ OH + M	(termination)
RXN21: H + OH + M ↔ H ₂ O + M	(termination)

At high pressure and low temperature conditions, the formation of the HO₂ radical becomes important (RXN 13-17). The HO₂ radical generates hydrogen peroxide (H₂O₂) radicals, which in turn produce OH radicals through the branching reactions (RXN 13-15). In addition, the HO₂ and atomic radicals contribute to the production of OH radicals (RXN 16, 17) resulting in a short-lived high concentration of OH radicals. From this set

of reactions it is easy to see that the HO_2 radical produces OH, which can then react with more HO_2 (RXN 11) to produce H_2O product. Thus, the HO_2 radical can both initiate and sustain the termination process.

Molecular dissociation is a significant effect for a stoichiometric hydrogen/oxygen flame. Dissociation reactions have high activation energies, resulting in very sensitive temperature variations. Hence, the dissociation of the reactants results in H and O radicals at low pressure and high temperature conditions. These highly reactive radicals very quickly form stable molecules such as H_2 , O_2 , and H_2O and OH radicals by several recombination processes (RXN 18-21).

In particular, the conditions of interest in this study are the ZND post-shock conditions, which exist at high temperatures and pressures. The HO_2 reaction processes (RXN 13-17) occur during the induction process, but the temperature due to the shock-compression is not high enough to induce dissociation. Thus, the high temperature mechanism mentioned above cannot be reliably applied to an induction zone. In fact, the ZND reaction processes mainly rely on the chain-branching and HO_2 reaction mechanism.

Structure of $\text{H}_2\text{-O}_2$ ZND Detonation

The $\text{H}_2\text{-O}_2$ reaction mechanism was used in the simulation tool described here to compute the post-shock condition within a ZND detonation wave. The equilibrium calculation estimated the Mach number of the stoichiometric CJ $\text{H}_2\text{-O}_2$ detonation to be 5.3. This structure - the leading shock wave, the subsequent high pressures and temperatures, and the ensuing reaction zone - results in the ZND reaction mechanism.

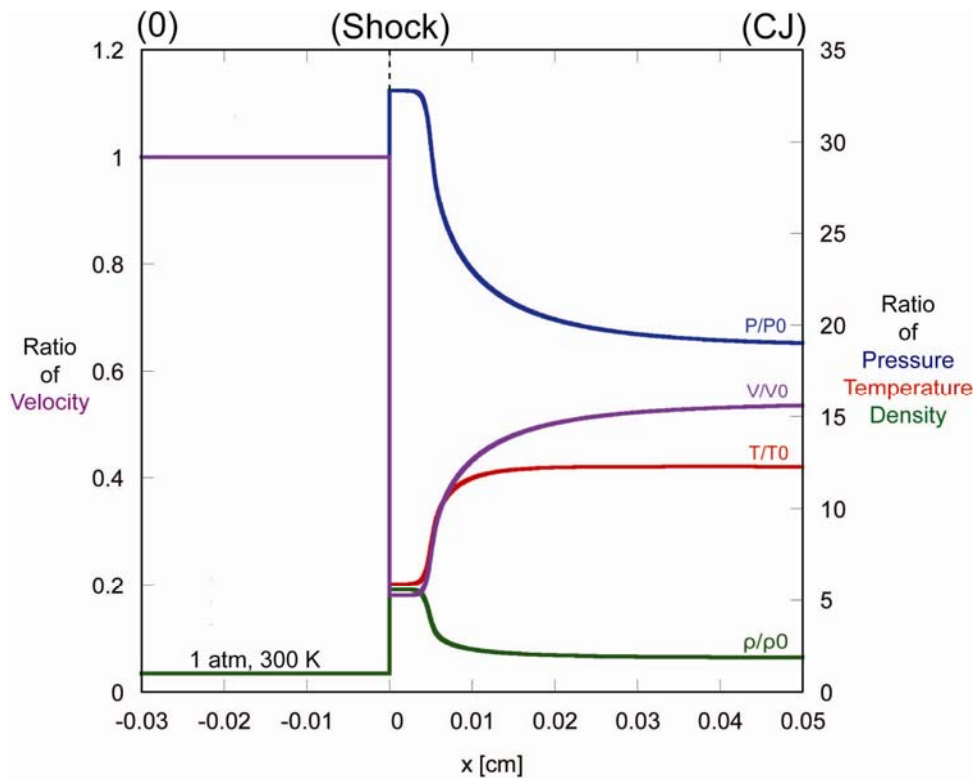


Figure 5.1. Thermodynamic properties and velocity of the ZND detonation (Initial P : 1 atm, T : 300 K, M : 5.3)

Using the methodology presented herein, this reaction mechanism produces the following results. Figure 5.1 shows the variations of physical properties through a stoichiometric hydrogen/oxygen ZND detonation wave. Note the artificially imposed discontinuous jump due to shock compression. In the subsequent attached reaction zone, all physical property values vary smoothly from the von Neumann state to the CJ state.

The mixture's thermodynamic properties exhibit the opposite trend of velocity in the reaction zone of a CJ detonation. There is a plateau behind the inviscid shock wave, associated with the induction zone of the detonation, which can be attributed to the chemical initiation reactions. Reaction rates slowly increase in the region behind the shock wave, resulting in a continuous slow temperature increase. In fact, the large heat

release due to the branching and termination reactions cannot take place until the radical concentrations are high enough. This finite amount of time needed is the induction time. In a steady state system, this results in a finite distance, termed the induction length, by which the reaction zone trails from the shock wave while the radical concentrations increase to yield explosion. This is evident in the simulation through the profiles of all physical properties which remain nearly constant in the region after the shock. One can see from Figure 5.1 that the induction length is very thin (approximately 40 μm), corresponding to an induction time of approximately 8 ns. Once explosion happens, the temperature of the mixture rapidly increases to the CJ temperature, and all other physical properties also move towards the CJ state.

Table 5.2. Pressure differences between an experimental and calculated result

<p>Peak Pressure 27 atm (experiment Ref.28) 34 atm (ZND calc.)</p> <p>Equilibrium Pressure 19 atm (experiment Ref. 28) 19 atm (ZND calc. CJ point)</p>
--

As shown in Table 5.2, the peak pressure of our hydrogen/oxygen ZND calculation is 25% higher than experimental values [27]. Since the ZND model is the simplest representation of a detonation wave, the simulation does not include wall friction, heat transfer effects, or mass transport.

Figure 5.2 shows the temperature profile and mass fractions for the CJ hydrogen/oxygen detonation wave. The combustion of $\text{H}_2\text{-O}_2$ generates hydrogen and oxygen radicals in

the high temperature region. However, it is slightly easier to dissociate H_2 than O_2 , hence H radicals appear faster than O radicals. Then, the hydroxyl radical concentration rapidly increases when chain branching occurs.

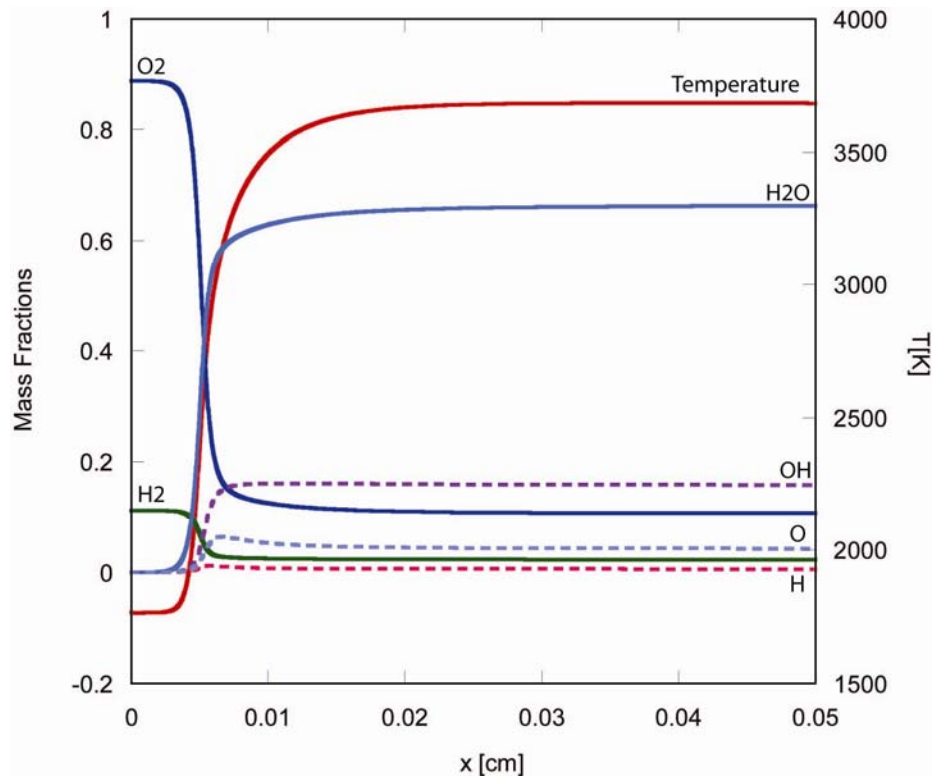


Figure 5.2. Temperature and species mass fractions in the reaction zone

As the final equilibrium state is reached, the mass fraction of hydroxyl remains quite high (0.18). Since the H_2 - O_2 mixture has a very high equilibrium temperature, the dissociation of the products occurs even at the final CJ state (RXN 16). Moreover the hydroperoxyl radicals generate hydroxyl radicals through the final oxidation process (RXN 9) which also causes high OH mass fractions at equilibrium.

Structure of H₂-Air ZND Detonation

Figure 5.3 shows the pressure and temperature change of both the hydrogen/oxygen and the hydrogen/air ZND detonations. The structure of a hydrogen/air reaction zone is similar to that of a hydrogen/oxygen reaction zone. However, the induction of the hydrogen/air mixture is five times longer than that of the hydrogen/oxygen mixture. Another characteristic of the hydrogen/air ZND detonation is that the thermodynamic properties at the von Neumann and equilibrium states are lower than for the equivalent hydrogen/oxygen system.

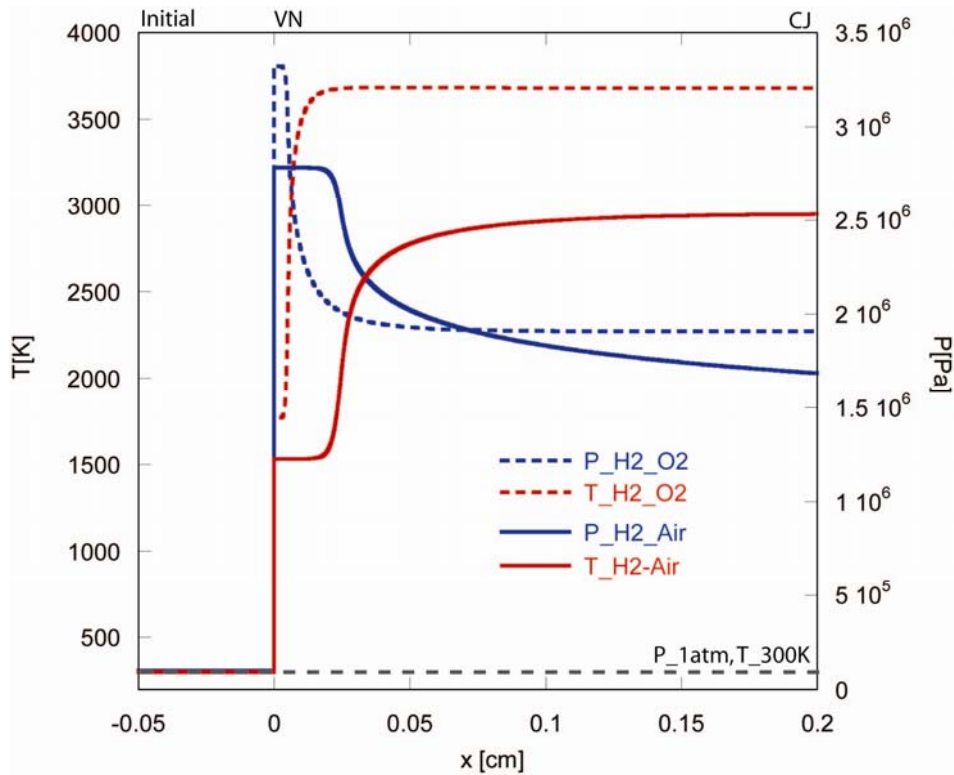


Figure 5.3. The CJ detonation of hydrogen/oxygen and hydrogen/air mixture

In stoichiometric hydrogen/air mixtures, the nitrogen (N_2) molecules are the dominant species because air is composed of 78% inert nitrogen molecules. After the shock compression, numerous nitrogen molecules inertly collide with hydrogen and oxygen molecules, and this delays the chain-branching reactions. In fact, the reaction rates of the final oxidation of hydrogen become slower than those of the hydrogen/oxygen system. Therefore, the induction plateau of a mixture longer than that of the hydrogen/oxygen system. Lower temperatures at the CJ state are due to the presence of N_2 . The presence of inert N_2 reduces the equilibrium adiabatic temperature of a hydrogen/air detonation: less enthalpy is available for heating the products, since N_2 contributes no enthalpy of formation.

According to Table 5.3, the ZND detonation velocity of hydrogen/air is lower than that of hydrogen/oxygen reactions. The hydrogen/air mixture has a large initial detonation velocity because the CJ condition is sonic at equilibrium state, the combination of different fuel and oxidizers need an unequal detonation velocity.

Table 5.3. Comparison of physical properties between H_2-O_2 and H_2 -Air Detonation, no equivalent accuracy should be inferred

<p>Detonation Velocity 2836 m/s (CJ. $H_2 - O_2$) 1969 m/s (CJ. $H_2 - Air$)</p>
<p>Post-shock Pressure 32.8 atm (CJ $H_2 - O_2$) 27.4 atm (CJ. $H_2 - Air$)</p>
<p>Post-shock Temperature 1765 K (CJ. $H_2 - O_2$) 1531 K (CJ. $H_2 - Air$) $\Delta T = 233$ K</p>

Figure 5.4 shows pressure-specific volume (P - v) diagrams of hydrogen/oxygen and hydrogen/air detonations. According to the figure, the density of hydrogen/air system is higher than that of hydrogen/oxygen since the two systems have different chemical compositions at initial states. If the density of hydrogen/air has the same density as that of hydrogen/oxygen system, and both initial states are identical, then the slope of hydrogen/oxygen should be larger because the detonation velocity of hydrogen/oxygen is faster than that of hydrogen/air, as shown in Table 5.3. In fact, the hydrogen/oxygen CJ detonation obtains higher pressure and temperature after the shock compression. As the reaction rates follow the Arrhenius law, the lower post-shock temperature extends the induction length of the hydrogen/air detonation.

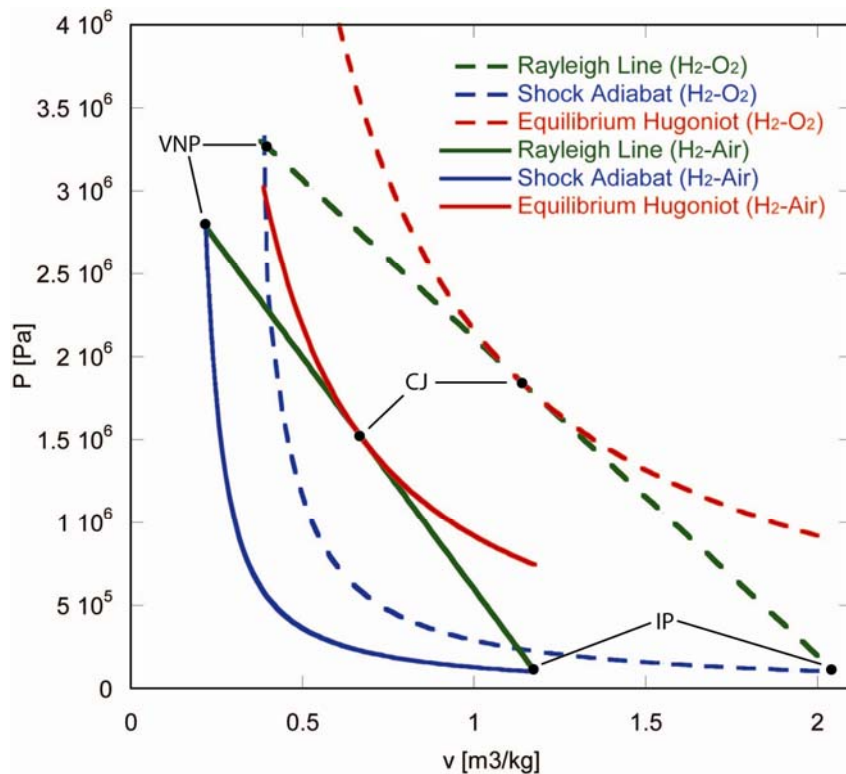
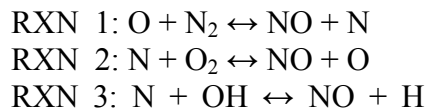


Figure 5.4. P - v diagrams of hydrogen/oxygen and hydrogen/air detonations

One last difference between the hydrogen/oxygen and hydrogen/air reaction mechanisms is the possibility for NO_x species generation when atmospheric nitrogen is present. There are three mechanisms by which nitrogen and oxygen combine to form NO_x: thermal, prompt, and fuel NO_x production mechanisms [28]. The thermal NO_x production mechanism takes place when a large heat release results in a chemical combination of atmospheric nitrogen and atmospheric oxygen. The prompt NO_x production mechanism occurs when hydrocarbon fuels combine with atmospheric nitrogen. The fuel NO_x production mechanism occurs when nitrogen atoms present in the fuel combine with atmospheric oxygen. In hydrogen/air reactions, fuel and prompt NO_x reactions cannot happen; only the thermal NO_x mechanism, as shown in Table 5.4, will occur according to the following reactions:

Table 5.4. Details of thermal NO_x reaction mechanism



The Zel'dovich thermal NO_x mechanism consists of three chain propagation reactions: (1) highly reactive oxygen radicals react to nitrogen molecules, (2) nitrogen radicals react to oxygen molecules, and (3) nitrogen radicals react to hydroxyl radicals. Each reaction must overcome high activation energies; therefore, the thermal mechanism is highly sensitive to temperature and becomes active for temperatures above 1800 K.

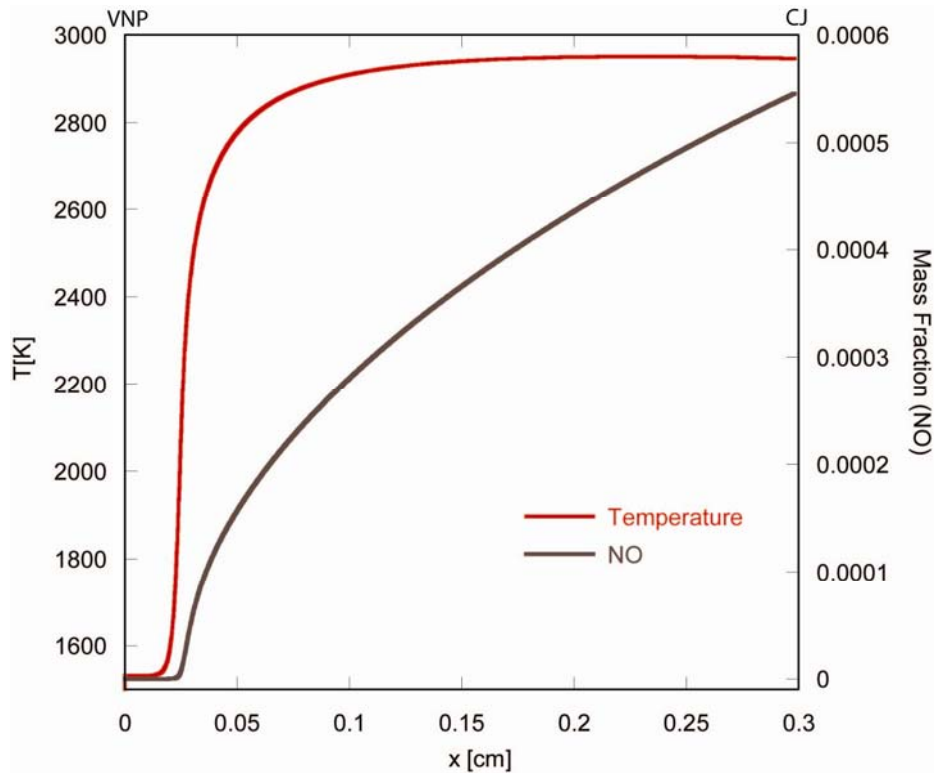


Figure 5.5. Mass fraction of NO and temperature for a hydrogen/air detonation

As shown in Figure 5.5, the NO mass fraction takes the value of 5.5×10^{-4} at the final CJ state. Thus, the NO_x mechanism does not contribute substantially to the differences between the hydrogen/air detonations.

Comparison between Full and Reduced $\text{H}_2\text{-O}_2$ Reaction Mechanisms

The hydrogen and oxygen reaction mechanism has been studied by many researchers. At Los Alamos Scientific Laboratory (LASL, the former name of Los Alamos National Laboratory), Bird and his colleagues developed a FORTRAN code for computing normal shock and reactive flow in gases [29]. Any reactive mixture could be simulated by two distinct computer programs: ‘HUG,’ which calculates the shock wave and Chapman-Jouguet (CJ) states, and ‘KIN,’ which integrates the rate equations to obtain a

steady-state solution. The KIN program uses reduced chemical kinetics of 9 species and 12 reactions for the hydrogen/oxygen/argon ZND detonation wave. The present work achieves a similar result by using the Cantera shock and detonation tool box to calculate the von Neumann and equilibrium states, while using an ODE integrator with the detailed chemical kinetics of GRI 3.0 with 53 species and 325 reactions.

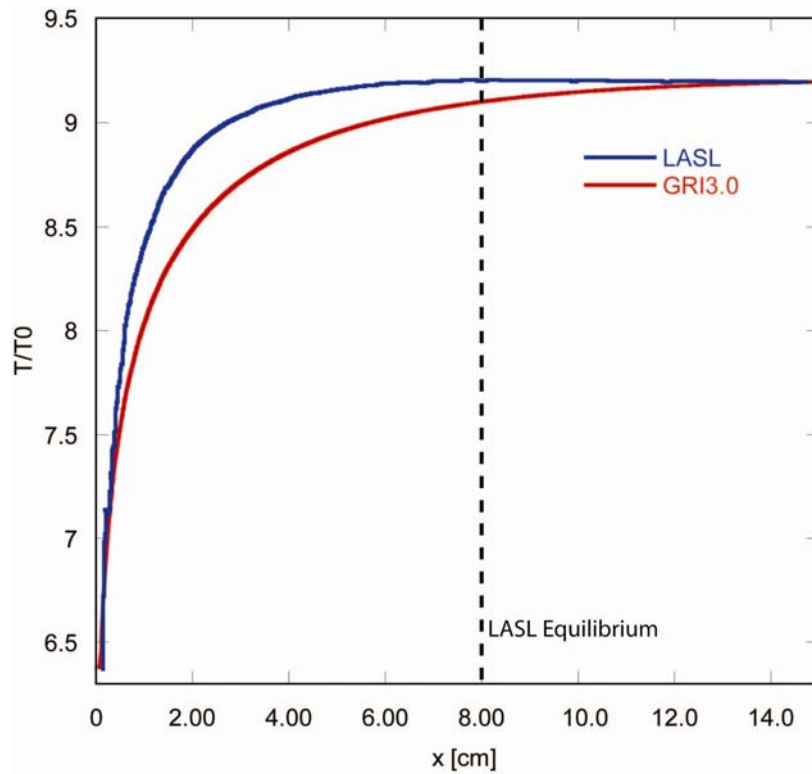


Figure 5.6. $2\text{H}_2 + \text{O}_2 + 9\text{Ar}$ CJ detonation: GRI 3.0 reaction mechanism compared to KIN reaction mechanism

Figure 5.6 shows the temperature profile for the $\text{H}_2\text{-O}_2\text{-Ar}$ detonation, computed using LASL and GRI 3.0 kinetics. The initial condition is set at standard pressure and temperature ($P_0 = 1$ atm, $T_0 = 300$ K) with a CJ detonation velocity of $D = 1572$ m/s,

analytically computed by Cantera shock and detonation tool box¹. Note that all physical properties at the VNP, i.e. after the shock compression, are identical for both the LASL and GRI-3.0 detonations. The results of the reaction zone calculation, however, are slightly different: the temperature of the LASL reaction mechanism reaches the CJ temperature faster than it does with the GRI 3.0 (Figure 5.6).

Table 5.5 lists all hydrogen/oxygen/argon reactions of the LASL code. In the initiation process (RXN 5), the hydrogen and oxygen molecules directly generate two hydroxyl molecules; such reactions that lead from two stable molecules to two radical species cannot be true elementary steps. Indeed, it would be difficult to accomplish the breaking of two homonuclear bonds and the formation of two heteronuclear ones in a single step. Instead, the GRI-3.0 kinetic scheme is based on a more detailed reaction mechanism, which incorporates more reactions to generate hydroxyl molecules. According to the hydrogen/oxygen reaction mechanism in Table 5.5, the hydroxyl radicals begin forming the product water (H₂O) molecules through RXN 3 & 4.

Table 5.5. Reaction mechanism of LASL program for H₂-O₂-Ar reaction

RXN 1: H + O ₂ ↔ OH + O	(branching)
RXN 2: H ₂ + O ↔ OH + H	(branching)
RXN 3: H ₂ + OH ↔ H ₂ O + H	(propagation)
RXN 4: OH + OH ↔ H ₂ O + H	(termination)
RXN 5: M + H ₂ + O ₂ ↔ 2OH + M	(initiation)
RXN 6: H + H + Ar ↔ H ₂ + Ar	(termination)
RXN 7: H + H + H ₂ O ↔ H ₂ + H ₂ O	(termination)
RXN 8: H + O ₂ + Ar ↔ HO ₂ + Ar	(propagation)
RXN 9: H + O ₂ + H ₂ O ↔ HO ₂ + H ₂ O	(propagation)
RXN10: H + OH + Ar ↔ H ₂ O + Ar	(termination)
RXN11: H + OH + H ₂ O ↔ 2H ₂ O	(termination)
RXN12: OH + HO ₂ ↔ H ₂ O + O ₂	(termination)

¹ It should be noted that despite the use of 4 and 5 digits in the description of observables (such as *D*) no equivalent accuracy should be inferred. For example, the detonation velocity of a planar H₂-O₂ detonation would be approximately 1600 m/s, if such a one-dimensional system could be generated in practice.

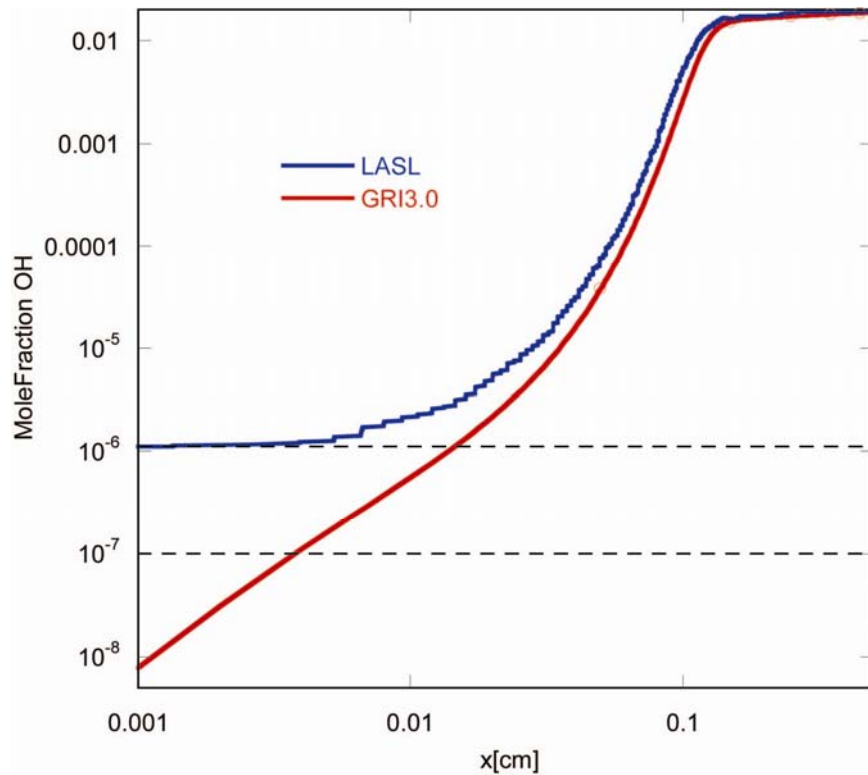


Figure 5.7. OH mole fraction for LASL and GRI kinetic mechanisms in a reaction zone

Figure 5.7 shows the mole fractions of hydroxyl radicals for the LASL and GRI-3.0 reaction mechanisms. The mole fraction of hydroxyl for the GRI-3.0 mechanism increases from 10^{-8} to 10^{-6} in the induction zone. Then, the chain-branching reactions cause the temperature to increase exponentially up to the CJ state. Since the LASL mechanism has faster hydroxyl generation, the branching reaction also begins sooner than with the GRI-3.0 mechanism. The difference between the hydroxyl mole fractions indicates that the temperature increases faster with the LASL reaction mechanism than with the GRI-3.0 mechanism (steeper slope).

CH₄-O₂ Reaction Mechanism

Table 5.6 shows the main reactions in the methane/oxygen system. At low temperature conditions, the chain-initiation step occurs through the reaction of stable methane and oxygen molecules and generation of methyl (CH₃) and hydroperoxyl (HO₂) radicals (RXN 1). At high temperatures, the methane molecule reacts with dissociated H, O, and OH radicals (RXN 2-4) to produce more methyl radicals.

At low temperatures, formaldehyde (CH₂O) can form directly from the reaction of methyl radicals and oxygen molecules (RXN 5). At this point, rapid oxidation of methyl radicals would require a sufficient concentration of oxygen molecules at high temperatures. If there is an insufficient oxygen concentration in the reacting mixture, the methyl radicals will react with the oxygen radicals (instead of reacting with oxygen molecules) to form formaldehyde (RXN 6).

The formaldehyde produced by RXN 5 or 6 can be further broken down to produce formyl (CHO) radicals by several different chain branching reactions (RXN 7-9). The CHO radicals will rapidly react with oxygen or M (any stable gas molecule) to generate carbon monoxide (CO) (RXN 10-11). Carbon-monoxide is a critical factor for the final oxidation processes to generate carbon dioxide (CO₂).

There are several reactions that generate CO₂ molecules from CO (RXN 12 – 14). Referring back to the hydrogen/oxygen reaction mechanism, it was seen that a high concentration of hydrogen radicals is a good indicator of a high overall reaction rate. Similarly, for the methane/oxygen reaction, formaldehyde concentrations are a good indicator of the overall reaction rate.

Table 5.6. Main reactions and mechanism of methane/oxygen combustion

RXN 1: $\text{CH}_4 + \text{O}_2 \leftrightarrow \text{CH}_3 + \text{HO}_2$	(Initiation)
RXN 2: $\text{CH}_4 + \text{H} \leftrightarrow \text{CH}_3 + \text{H}_2$	(propagation)
RXN 3: $\text{CH}_4 + \text{O} \leftrightarrow \text{CH}_3 + \text{OH}$	(branching)
RXN 4: $\text{CH}_4 + \text{OH} \leftrightarrow \text{CH}_3 + \text{H}_2\text{O}$	(propagation)
RXN 5: $\text{CH}_3 + \text{O}_2 \leftrightarrow \text{CH}_2\text{O} + \text{OH}$	(propagation)
RXN 6: $\text{CH}_3 + \text{O} \leftrightarrow \text{CH}_2\text{O} + \text{H}$	(termination)
RXN 7: $\text{CH}_2\text{O} + \text{O}_2 \leftrightarrow \text{CHO} + \text{HO}_2$	(branching)
RXN 8: $\text{CH}_2\text{O} + \text{HO}_2 \leftrightarrow \text{CHO} + \text{H}_2\text{O}_2$	(branching)
RXN 9: $\text{CH}_2\text{O} + \text{CH}_3 \leftrightarrow \text{CHO} + \text{CH}_4$	(propagation)
RXN10: $\text{CHO} + \text{O}_2 \leftrightarrow \text{CO} + \text{HO}_2$	(propagation)
RXN11: $\text{CHO} + \text{M} \leftrightarrow \text{CO} + \text{H} + \text{M}$	(propagation)
RXN12: $\text{CO} + \text{O}_2 \leftrightarrow \text{CO}_2 + \text{O}$	(branching)
RXN13: $\text{CO} + \text{OH} \leftrightarrow \text{CO}_2 + \text{H}$	(propagation)
RXN14: $\text{CO} + \text{H}_2\text{O} \leftrightarrow \text{CO}_2 + \text{H}_2$	(termination)

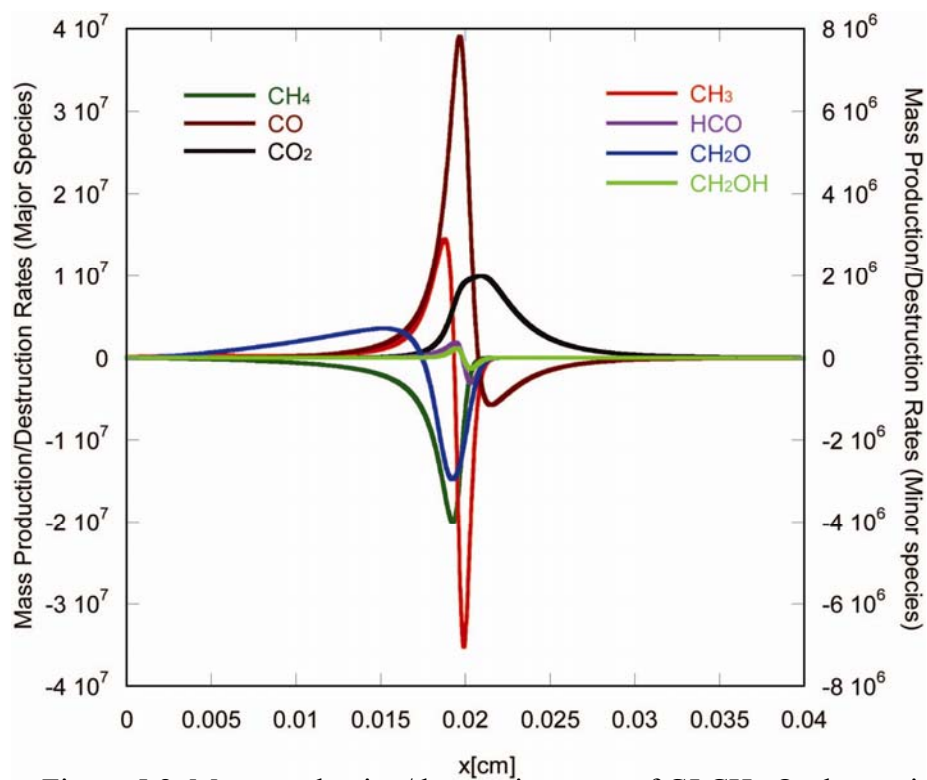
Figure 5.8. Mass production/destruction rates of CJ $\text{CH}_4\text{-O}_2$ detonation

Figure 5.8 shows the mass production/destruction rates for certain major and minor species. In the induction zone, CH_3 radicals cannot sustain themselves and immediately react to generate CH_2O . Once the temperature becomes high enough, CH_3 is retained because of a large CH_4 decomposition reaction. However, CH_3 will be completely consumed when all the CH_4 is depleted during the reaction.

Structure of $\text{CH}_4\text{-O}_2$ ZND Detonation

Figure 5.9 shows the pressure profile of the CJ methane/oxygen detonation through the reaction zone.

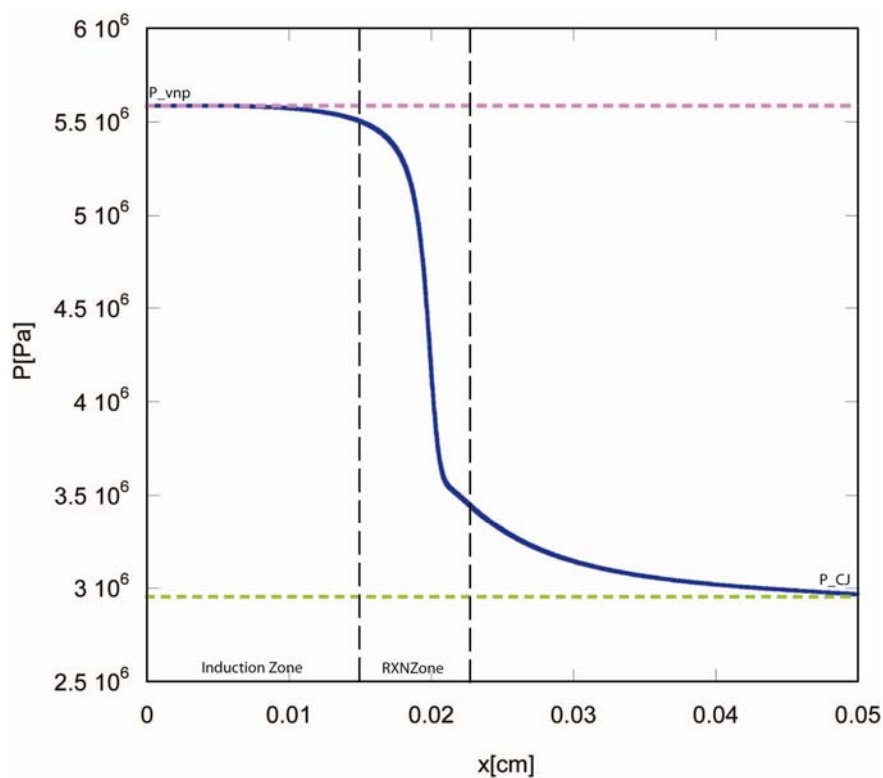


Figure 5.9. Pressure contour for the CJ detonation of stoichiometric $\text{CH}_4\text{-O}_2$ reaction (Initial P : 1 atm, T : 300 K)

Pressure sharply decreases from its value at the von Neumann point to the CJ condition. The pressure path of the methane/oxygen ZND detonation is similar to that of the hydrogen/oxygen case, but the induction length of methane/oxygen detonation is longer than that of hydrogen/oxygen detonation by approximately a factor of four ($\text{CH}_4\text{-O}_2$: 150 μm , $\text{H}_2\text{-O}_2$: 40 μm). This is expected since methane, a more complicated molecule, needs to be broken down to many intermediate species, while the $\text{H}_2\text{-O}_2$ system is a sub-system of the $\text{CH}_4\text{-O}_2$ mechanism.

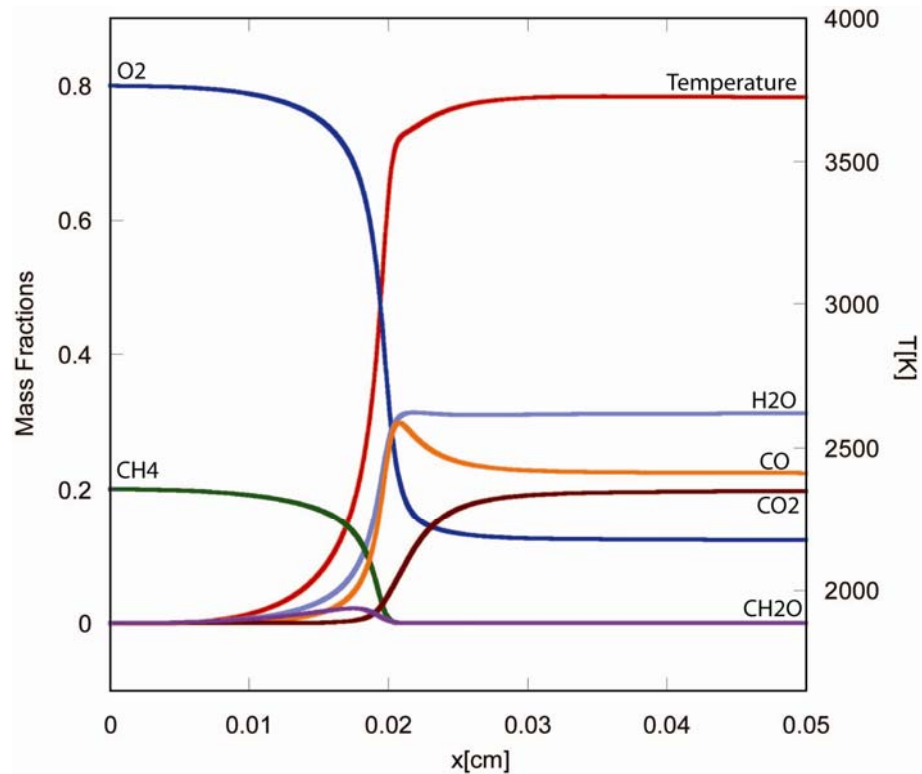


Figure 5.10. Temperature and mass fractions of main species in the reaction zone for the CJ detonation of stoichiometric $\text{CH}_4\text{-O}_2$ mixture (Initial P : 1 atm, T : 300 K)

Figure 5.10 shows the temperature and selected mass fractions for the CJ methane/oxygen detonation wave. At the post-shock state, the high temperature results

in a modest reaction, which in turn changes the initial compositions of methane and oxygen molecules. At the same time the temperature is not high enough to induce dissociation or activate the high reaction rates of the high-temperature oxidation mechanism. The breakdown of the reactants slowly generates methyl and other reactive radicals (RXN 1-4), which quickly react to form formaldehyde; thus, the behavior of the mass fractions of formaldehyde coincides with the increase in methane consumption. Carbon monoxide is generated by the chain-branching and propagation reactions through the formyl reactions (RXN 10-11). The final oxidation of the $\text{CH}_4\text{-O}_2$ reaction occurs when enough carbon monoxide molecules have been generated such that RXN 12-14 activate and produce CO_2 . These exothermic reactions finally raise the temperature to the Chapman-Jouguet state. When the methane molecules are completely consumed, the temperature slowly converges to the Chapman-Jouguet state, and the remaining carbon monoxide molecules appear in the equilibrium products.

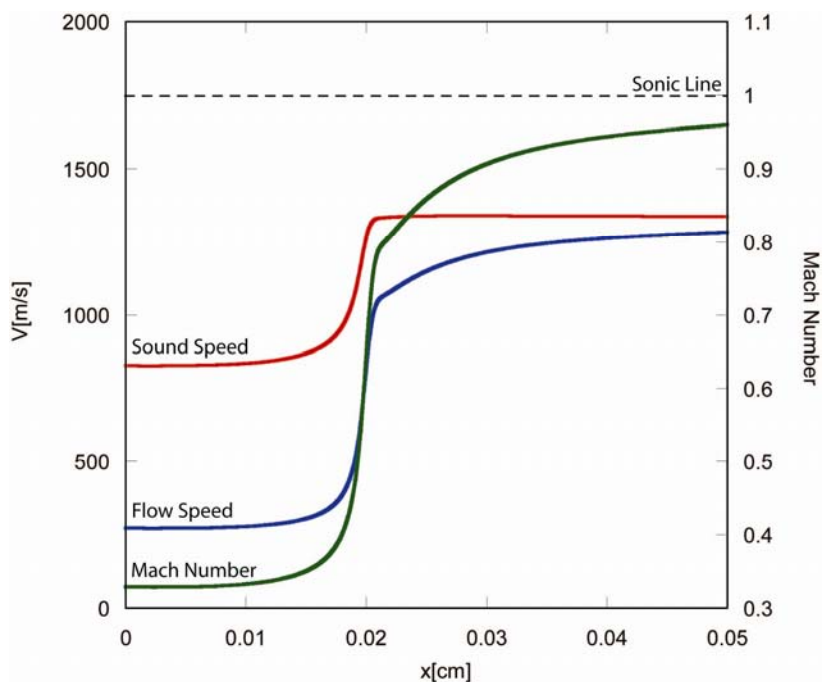


Figure 5.11. Velocity, sound speed, and Mach number in the reaction zone for the CJ detonation of stoichiometric $\text{CH}_4\text{-O}_2$ mixture (Initial P : 1 atm, T : 300 K)

Figure 5.11 shows the relationships between flow speed, sound speed, and Mach number for the methane/oxygen CJ detonation wave. The flow velocity after shock compression is subsonic (Mach = 0.33). In the induction zone, the velocity increases as the density of the mixture decreases due to the reaction. The sound speed is primarily a function of temperature ($[\gamma RT]^{1/2}$ for the equilibrium speed of sound), and hence $[\gamma RT]^{1/2}$ increases as the temperature increases.

Structure of CH₄-Air ZND Detonation

Figure 5.12 shows the pressure and temperature change of both methane/oxygen and methane/air mixtures in the ZND reaction zone. The structure of the methane/air reaction zone is similar to that of the methane/oxygen reaction. As in the hydrogen/air mechanism, temperatures at von Neumann and CJ states are lower, and the induction length is 100 times longer than that of methane/oxygen ones.

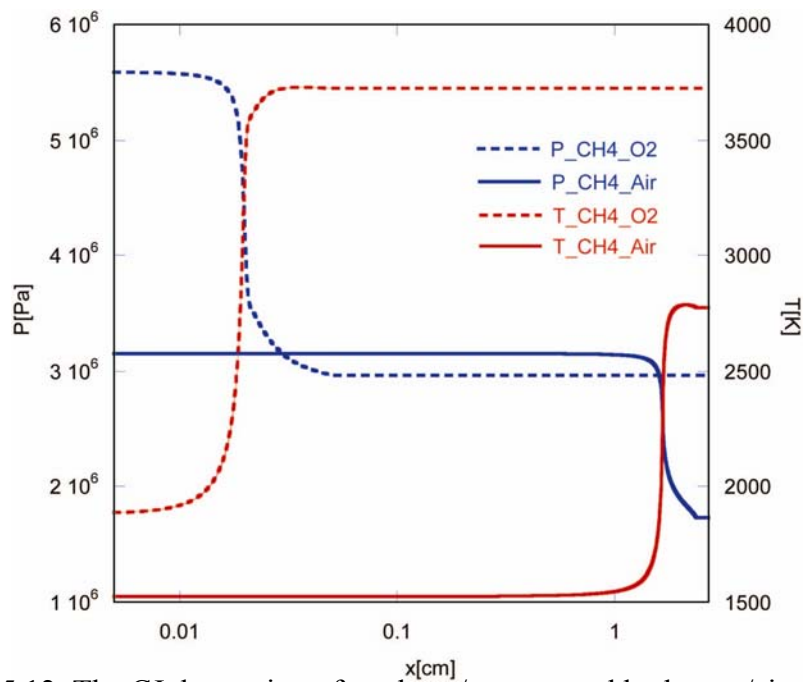


Figure 5.12. The CJ detonation of methane/oxygen and hydrogen/air mixture

The longer induction length of methane/air detonation is caused by lower temperature after shock compression and the inert collisions of reactive molecules with N_2 molecules. After the shock compression, a large number of nitrogen molecules inertly collide with methane and oxygen molecules, which delays the chain-branching reactions.

According to Table 5.7, the detonation velocity of methane/air is lower than that of methane/oxygen reactions. The initial pressure and temperature are identical in both cases, while the specific volumes are very close, yet the methane/oxygen mixture has a large detonation velocity².

Table 5.7. Comparison of physical properties between CH_4 - O_2 and CH_4 -Air Detonation, no equivalent accuracy should be inferred

<p>Detonation Velocity 2390 m/s (CJ. CH_4 - O_2) 1802 m/s (CJ. CH_4 - Air)</p>
<p>Post-shock Pressure 55.1 atm (CJ. CH_4 - O_2) 31.1 atm (CJ. CH_4 - Air)</p>
<p>Post-shock Temperature 1884 K (CJ. CH_4 - O_2) 1525 K (CJ. CH_4 - Air) $\Delta T = 359$ K</p>

² It should be noted that this is a clear difference between hydrogen fuel detonations and methane fuel detonations. The first one exhibits large density and specific volume sensitivity to the presence of nitrogen while the second one does not. This is clearly due to the large disparity between the molecular weights of hydrogen and all other species under consideration.

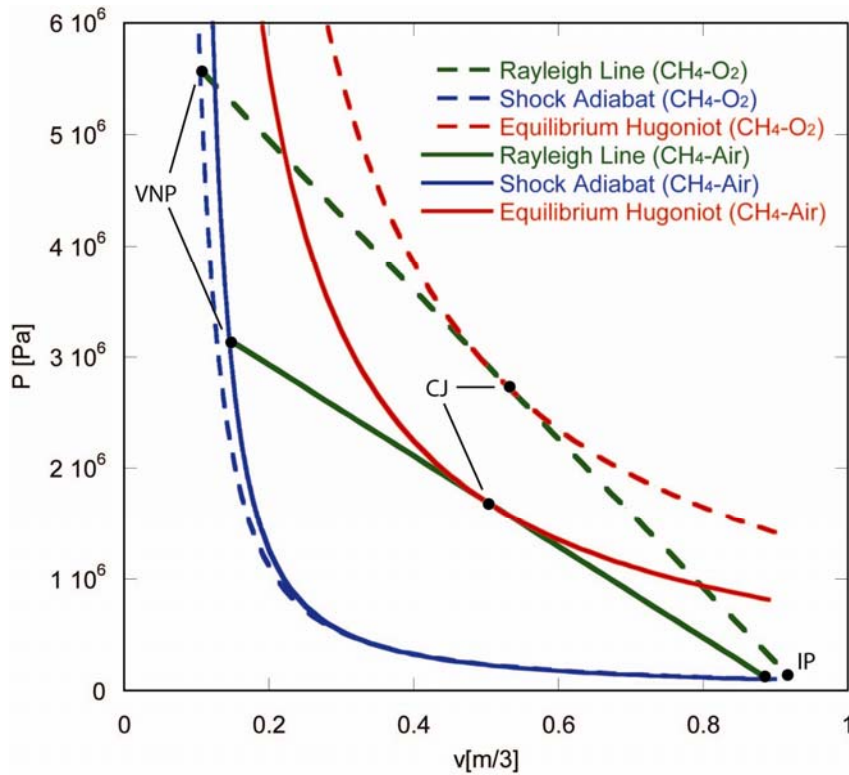


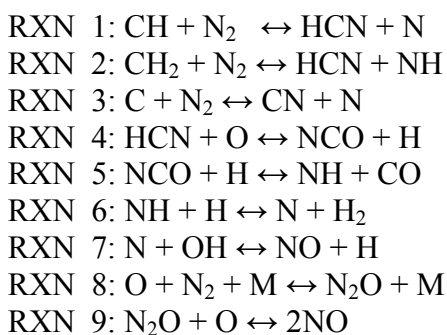
Figure 5.13. P - v diagrams of methane/oxygen and methane/air detonations

Figure 5.13 shows P - v diagrams of methane/oxygen and methane/air detonations. In this case, the initial states of a methane/air detonation are close to that of a methane/oxygen detonation. The slope of the methane/air Rayleigh line, which is associated with the detonation velocity, is lower than that of methane/oxygen. In fact, the pressure and temperature are also lower than that of the methane/oxygen case at the von Neumann and CJ states, as shown in Table 5.7. The presence of N_2 reduces the equilibrium adiabatic temperature of a methane/air detonation since N_2 acts as diluent in the system.

Like the hydrogen/air system, the thermal NO_x production mechanism is also active here at high temperature. The peak temperature (2780K) is lower than the temperatures at which N_2 dissociates, and as a result, the importance of thermal NO_x is reduced. For

CH₄, as well as for all other hydrocarbons, there exists an additional NO_x production mechanism, namely the prompt NO_x mechanism [30].

Table 5.8. Details of prompt NO_x reaction mechanism



At low temperatures, hydrocarbons react with N₂ to form hydrogen cyanides (HCN) in Table 5.8. There are two reactions to produce HCN from the CH₄ molecules: (1) the CH radicals react with N₂ to form HCN and N, (2) the CH₂ radicals react with N₂ to form HCN and NH. Since nitrogen radicals are generated through RXN 1, 3, and 6, the nitrogen radicals react with hydroxide to produce NO, as in the thermal NO_x production mechanism (RXN 7). At high temperatures, nitrous oxide (N₂O) also generates NO when oxygen radicals exist at sufficient concentrations.

Figure 5.14 shows the temperature and mass fraction of NO for a methane/air detonation. When temperature is not high enough, no NO is generated.

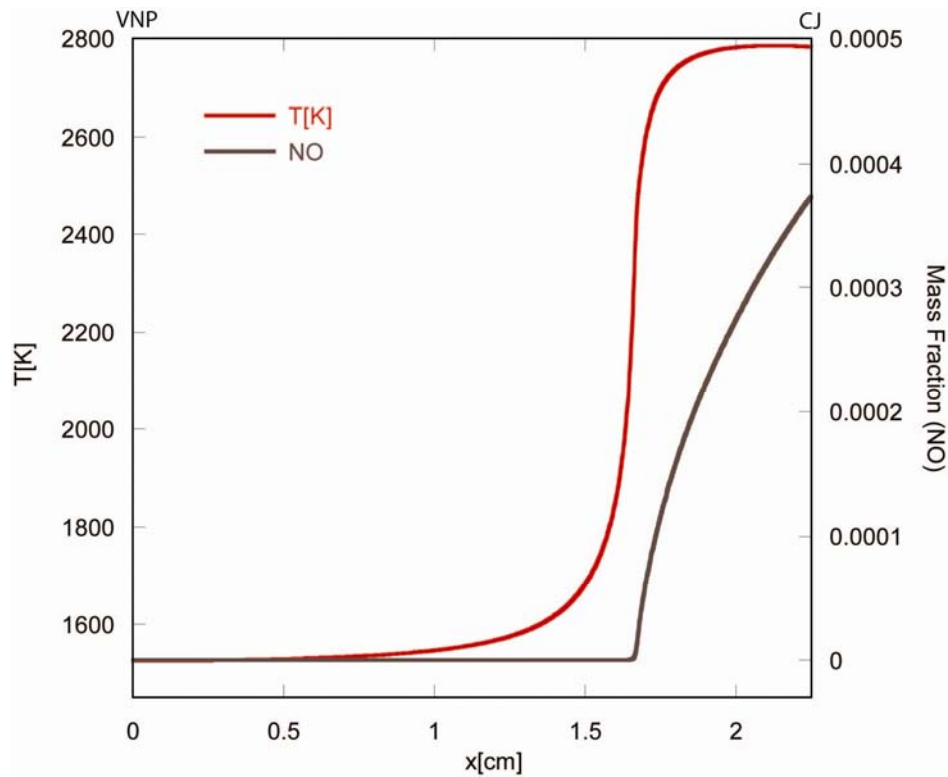


Figure 5.14. Mass fraction of NO and temperature for a methane/air detonation

When the combustion begins, NO increases to its final CJ value of 3.7×10^{-4} . In fact, the NO_x mechanism does not contribute substantially to temperature reduction.

Chapman-Jouguet and Overdriven Detonation on P - v Diagram

Figure 5.15 shows the computation of the reaction zone of a stoichiometric methane/oxygen CJ detonation on the P - v diagram. The slope of the computed line (purple line) exactly matches the slope of the Rayleigh line (green line) of the methane/oxygen CJ detonation because the total mass flux of the flow is constant throughout the entire process of the one-dimensional detonation.

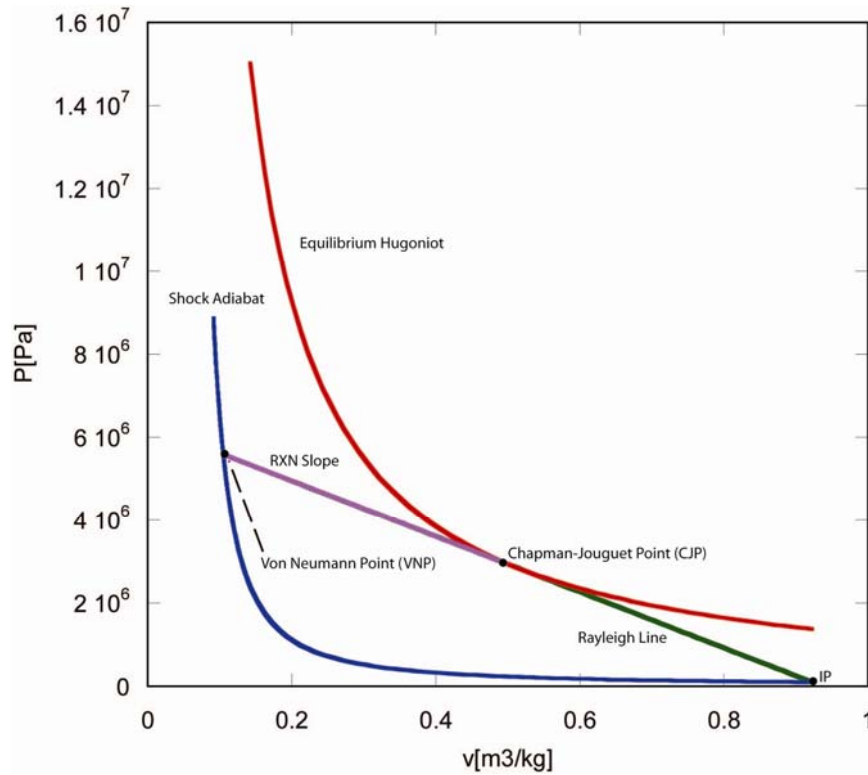


Figure 5.15. The CJ detonation of $\text{CH}_4\text{-O}_2$ reaction on a Rankine-Hugoniot diagram

An overdriven detonation occurs when a piston forcefully induces an additional velocity (from right to left) onto the detonation wave as shown in Figure 5.16. A strong overdriven detonation can be maintained by a piston whose velocity is independently controlled, thereby providing additional downstream velocity to the detonation wave.

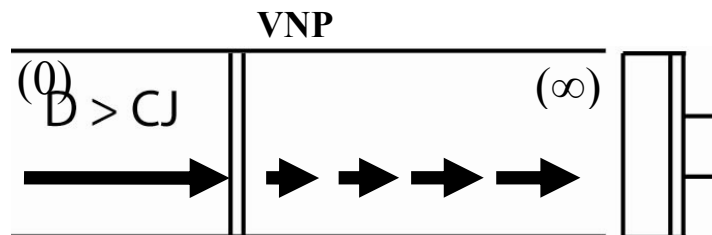


Figure 5.16. Schematic diagram of over-driven detonation by a piston

Since the supersonic shock wave compresses an unburnt incoming flow, the von Neumann point of an overdriven detonation is higher than for the case of the Chapman-Jouguet detonation. The slope of the Rayleigh line indicates a larger mass flux induced by the piston (Figure 5.17). A reaction slope always follows the Rayleigh line for any inviscid one-dimensional ZND detonation; therefore, the new final equilibrium point lies in the subsonic region of the equilibrium Hugoniot curve.

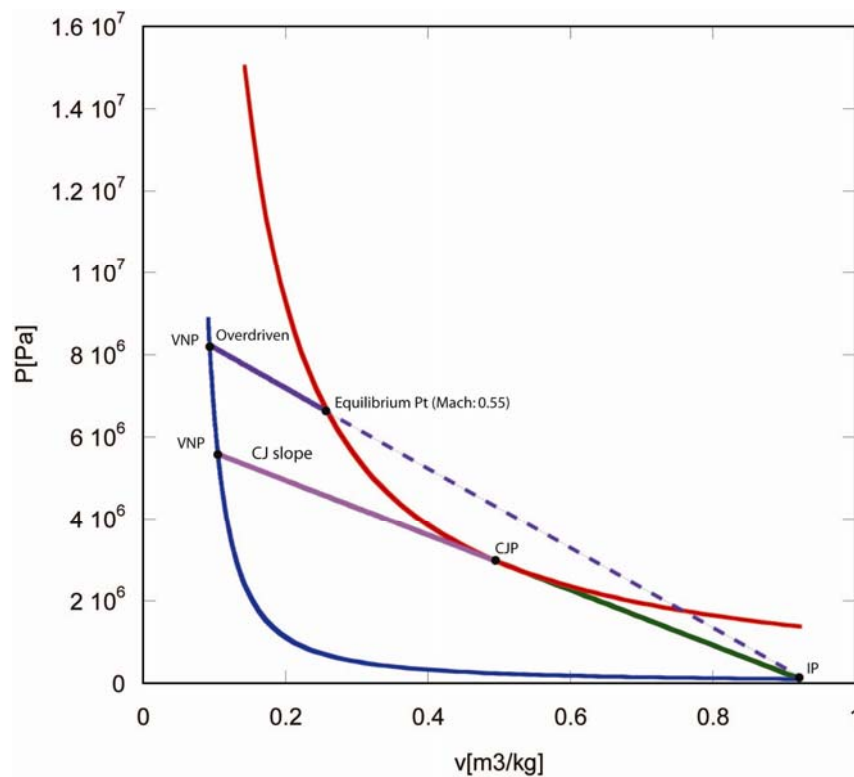


Figure 5.17. Comparison between an overdriven detonation ($M_{CJ} = 1.2$) and a Chapman-Jouguet detonation ($M_{CJ} = 1.0$) in P - v diagram

Mollier Diagrams

Figure 5.18 shows both thermal and chemical enthalpies due to the methane/oxygen ZND detonation. The Mollier diagram is a graphical representation of the relationship

between the enthalpy and entropy of the ZND detonation. The blue solid line in the Mollier diagram indicates the enthalpy change along the shock adiabat. The purple solid line represents the thermal and chemical components of the enthalpy change due to the reaction process along the Rayleigh line.

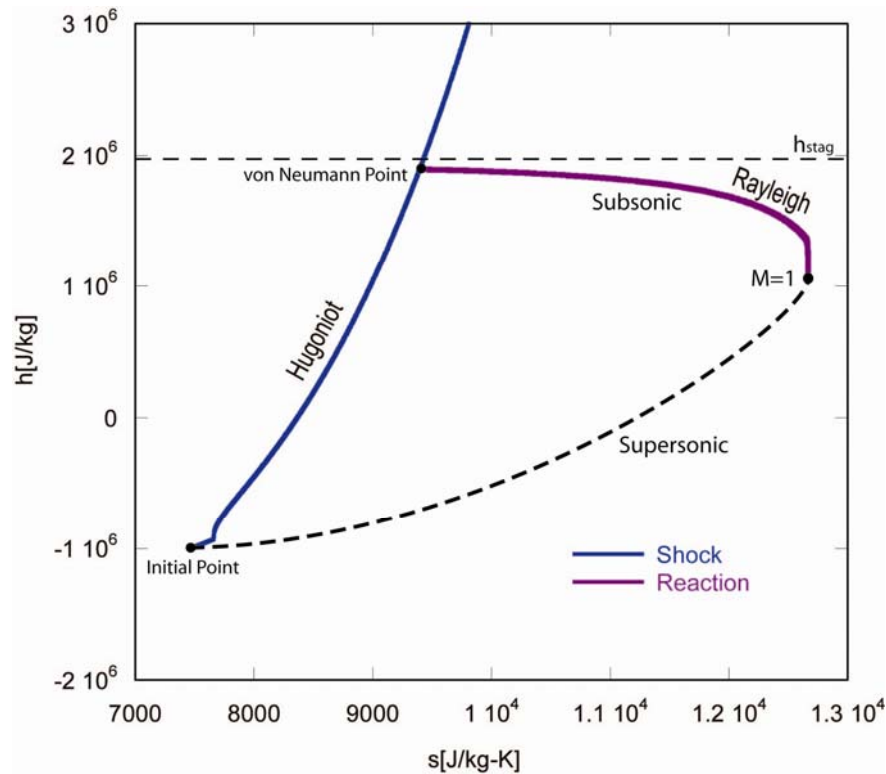


Figure 5.18. The Mollier diagram (h - s) of a CH_4 - O_2 Chapman-Jouguet detonation

According to the energy equations, the stagnation total enthalpy remains a constant throughout the ZND detonation structure. Thus, the difference between the stagnation enthalpy (h_{stag}) and the enthalpies along the Rayleigh trajectory is equal to the specific kinetic energy in the reaction zone.

The temperature of the mixture increases due to the reaction process (Figure 5.19), and as a result, the thermal enthalpy also increases, while the chemical enthalpy decreases due to the reaction. In fact, the overall enthalpy slightly decreases throughout the reaction, due to the acceleration inherent in the process from the VNP to the final equilibrium state.

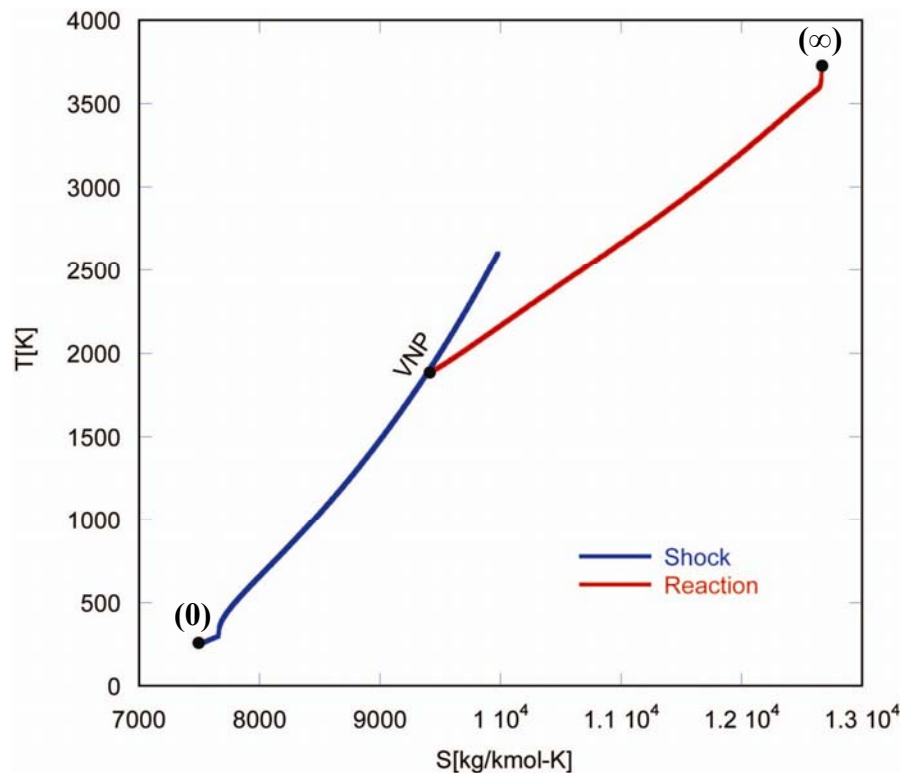


Figure 5.19. Temperature-Entropy diagram of a CH₄-O₂ Chapman-Jouguet detonation

According to the P - v diagram shown in Figure 5.15 the computational solution of the ZND detonation exactly matches the Rayleigh line up to the equilibrium state. However, the reaction follows only the subsonic region of the Rayleigh line. Thus, the Rayleigh line has another path that represents the supersonic region, which is a dashed line on Figure 5.19. This figure presents a T - s diagram, which can be useful in visualizing the

different causes of entropy increase through the detonation. As shown in the figure, the shock results in entropy increase due to irreversible compression, while the reaction results in entropy increase mostly through the difference in chemical potential between reactants and products. The entropy increase due to the reaction is stronger than the one due to the shock compression.

Differential Area Effect (Diffuser)

One straightforward application of the direct ODEs integration is the addition of an area function into the mass conservation equations. As shown in Figure 5.20, a diffuser can be made by linearly increasing the cross-sectional area of the one-dimensional detonation stream tube. The same numerical scheme presented in this study can be used to calculate a methane/oxygen detonation through a diffuser.

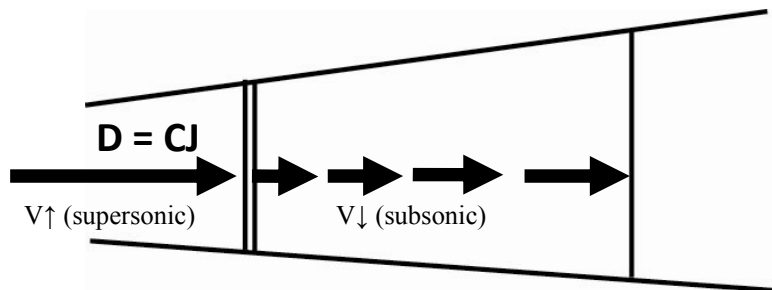


Figure 5.20. Chapman-Jouguet detonation through a diffuser

Figure 5.21 shows the result of a simple linear change in the diffuser area. The end tube area is linearly increased by 0.1%, 1%, 5%, and 10% of the initial cross-sectional area, while the distance between the changes was constant and equal to 0.2 cm. Since the reaction process of the methane/oxygen CJ detonation occurs within a very narrow region (much less than 0.1 cm), the slow linear area increase can only affect the pressure expansion substantially when most of the reactions are complete.

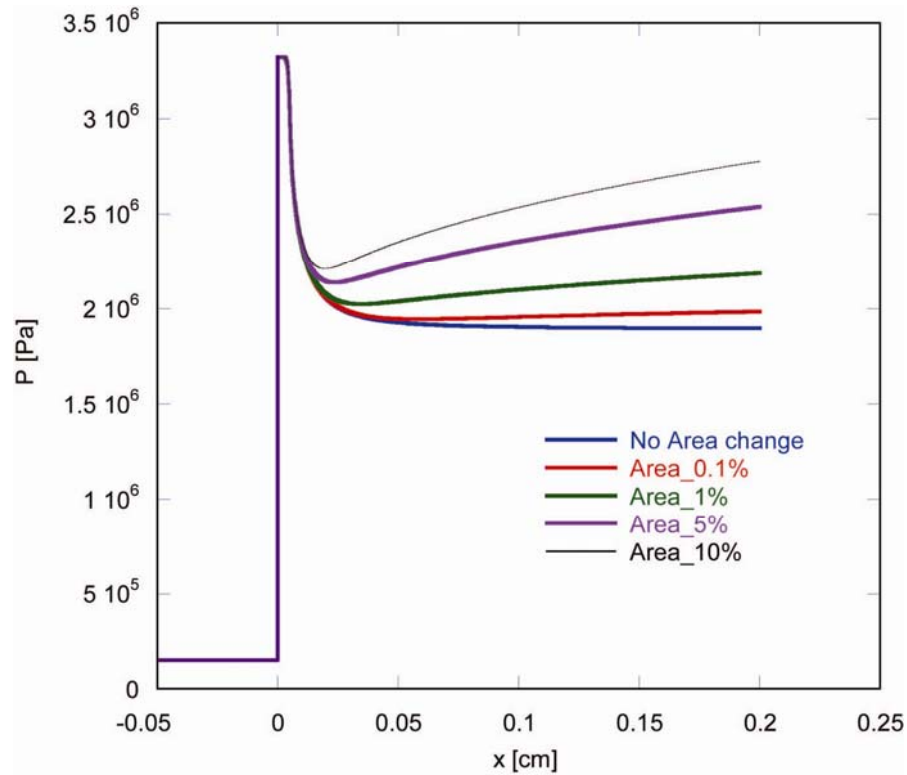


Figure 5.21. Pressure change using different diffuser cross-sectional areas

According to Figure 5.21, the flow expansion occurs after the reaction ends, and the pressure increase corresponds to the area increase. A good application for the area expansion is a bell-shaped nozzle configuration which offers rapid nozzle area increase. If the rate of area change is high enough in the initial stages of a reaction after the VNP state, the reactions may be affected, and the detonation may be “frozen” at some particular state.

Future Research

One possible future research direction includes the addition of wall friction forces or external heat transfer terms into the ODEs detonation integration. The equations would take the following form

Momentum equation:
$$P_0 + \rho_0 u_0^2 = P_1 + \rho_1 u_1^2 + \int \frac{\delta F}{A(x)}$$

Energy equation:
$$c_p T_0 + \frac{u_0^2}{2} + Q = c_p T_1 + \frac{u_1^2}{2} + \int \frac{\delta Q}{A(x)}$$

where δF is an effective wall friction force that represents the effect of the boundary layer, and δQ is an effective wall heat transfer term.

A more accurate detonation model should also include transport effects into the one-dimensional conservation equations [30]. The simpler case would be including a viscosity term into the conservation equations as

Momentum equation:
$$\frac{d}{dx} \left(P + \rho u^2 - \frac{4}{3} \mu \frac{du}{dx} \right) = 0$$

Energy equation:
$$\frac{d}{dx} \left[\rho u \left(h + \frac{1}{2} u^2 \right) - \frac{4}{3} \mu u \frac{du}{dx} \right] = 0$$

where μ is the kinematic viscosity. Other transport effects, such as heat conduction and mass diffusion, would be omitted from such a simple model [31, 32].

6. CONCLUSIONS

This thesis presents a computational simulation of the Zel'dovich-von Neumann-Doering detonation using detailed chemical kinetics and thermodynamics solvers.

The Zel'dovich-von Neumann-Doering detonation is the combination of an inviscid shock and a reaction zone. The flow through the inviscid shock results in algebraic jump equations that are numerically solved by using a Newton-Raphson iterative technique. In the reaction zone, the direct integration of ordinary differential equations with detailed chemical kinetics and thermodynamics provides a numerical solution of thermochemistry. The present work contributed knowledge about the calculation of the Zel'dovich-von Neumann-Doering detonation for four different fuel/oxidizer mixtures: $\text{H}_2\text{-O}_2$, $\text{H}_2\text{-Air}$, $\text{CH}_4\text{-O}_2$, and $\text{CH}_4\text{-Air}$. Computational results describe the behavior of thermochemistry, i.e. physical properties (pressure, velocity, temperature, etc), and mass fractions within a Zel'dovich-von Neumann-Doering detonation.

Future work will concentrate on including additional terms, such as wall friction, external heat transfer, and transport effects and should lead to a more accurate description of the detonation and ultimately contribute to the implementation of the transient inlet concept.

REFERENCES

- [1] Hill, P., Peterson, C., 1992, *Mechanics and Thermodynamics of Propulsion*, Addison-Wesley Publishing, Reading, MA, pp. 155-177.
- [2] Bussing, T., and Pappas, G., 1996, "Pulse Detonation Engine Theory and Concepts," *Developments in High-speed-vehicle Propulsion Systems*, **1**, pp. 421-472.
- [3] Lynch, E. D., and Edelman, R. B., 1996, "Analysis of Pulse Detonation Wave Engine.," *Developments in High-speed-vehicle Propulsion Systems*, **1**, pp. 473-516.
- [4] Strehlow, R. A., Adamczyk, A. A., and Stiles, R. J., 1972, "Transient Studies of Detonation Waves," *Astronautica ACTA*, **17**, pp. 509-527.
- [5] Moen, I., 1989, "Transition to Detonation in a Flame Jet," *Combustion and Flame* **75**, pp. 297-308.
- [6] Wingerden, K., and Bjerketvedt, D., 1994, "Detonation in Pipes and in the Open," Christian Michelsen Research (CMR) Report No. 843403-9.
- [7] Schultz, E., Wintenberger, E., and Shepherd, J., 1999, "Investigation of Deflagration to Detonation Transition for Application to Pulse Detonation Engine Ignition Systems," *16th JANNAF Propulsion Meeting*, Cocoa Beach, FL.
- [8] Zeldovich, Y. N., 1950, "On the Theory of the Propagation of Detonation in Gaseous Systems," *NACA Tech., Memo No. 1261*.
- [9] von Neumann, J., 1963, "Theory of Detonation Waves," *John von Neumann 1903-1957 Collected Works*, Pergamon Press, Oxford, England, Vol. 4, pp.203-218.
- [10] Doring, W.H., 1943, "On the Detonation Processes in Gases," *Ann. Phys.* **43**, pp. 421-436.
- [11] Glassman, I., 2008, *Combustion*, Academic Press, Burlington, MA, pp. 261-309.
- [12] Fickett, W., and Davis, C. D., 1979, *Detonation, Theory and Experiment*, University of California Press, Berkeley, CA, pp. 291-326.

- [13] Williams, F. A., 1985, *Combustion Theory*, Perseus Books Publishing, Reading, MA, pp. 521-647.
- [14] Kuo, K. K., 2002, *Principles of Combustion*, John Wiley & Sons, Hoboken, NJ, pp. 110-263.
- [15] Goodwin, D. G., 2003, "An Open-source, Extensible Software Suite for CVD Process Simulation," *Proceedings of CVD XVI and EuroCVD Fourteen, Electrochemical Society*, Delft, Netherlands, pp. 2038.
- [16] GRI-Mech 3.0 project overview, 2006, <http://www.me.berkeley.edu/gri-mech/overview.html#whatisgrimech>, 11/19/2009.
- [17] Law, C. K., 2006, *Combustion Physics*, Cambridge University Press, Cambridge, U.K., pp. 234-664.
- [18] Shepherd, J. E., 2009, "Detonation in Gases," *Proceedings of the Combustion Institute*, **32**, pp. 83-98.
- [19] Browne, S., Zeigler, J. and Shepherd, J. E., 2008, "Numerical Solution Methods for Shock and Detonation Jump Conditions," Technical Report FM 2004.004 GALCIT.
- [20] Browne, S., Liang, Z., and Shepherd, J. E., 2005, "Detailed and Simplified Chemical Reaction Mechanisms for Detonation Simulation," Paper 05F-21 of Western States Section of the Combustion Institute, Stanford University, Stanford, CA.
- [21] Kao, S., 2008, "Detonation Stability with Reversible Kinetics," Ph.D Thesis, California Institute of Technology, Pasadena, CA.
- [22] Kee, R. J., Coltrin, M. E., and Glarborg, P., 2003, *Chemically Reacting Flow, Theory and Practice*, John Wiley & Sons, Hoboken, NJ, pp. 661-682.
- [23] Brown, P. N., Byrne, G. D., and Hindmarsh, A. C., 1989, "VODE, A Variable-Coefficient ODE Solver," *SIAM Journal of Scientific and Statistical Computing*, **10**, pp. 1038-1051.
- [24] Oran, E. S., and Boris, J. P., 2000, *Numerical Simulation of Reactive Flow*, 2nd ed., Cambridge University Press, Cambridge, UK.

- [25] Cakmak, A. S., Botha, J. F., and Gray W. G., 1987, *Computational and Applied Mathematics for Engineering Analysis*, Springer-Verlag, Heidelberg, pp. 311-373.
- [26] Milne, W. E., 1970, *Numerical Solution of Differential Equations*, Dover Publications, Mineola, NY, pp. 25-218.
- [27] Edwards, D. H., Williams, G. T., and Breeze, J. C., 1959, "Pressure and Velocity Measurements on Detonation Waves in Hydrogen-oxygen Mixtures," *J of Fluid Mech.*, **6**, pp. 497-517.
- [28] Annamalai, K., and Puri, I. K., 2007, *Combustion Science and Engineering*, CRC press, Boca Raton, FL.
- [29] Bird, P. F., Duff, R. E., and Schott, G. L., 1964, "HUG, a FORTRAN-FAP Code for Computing Normal Shock and Detonation Wave Parameters in Gases," Los Alamos Research Scientific Laboratory Report No.LA-2980.
- [30] Hirschfelder, J. O., Curtis, C. S., Bird, R. B., 1964, *Molecular Theory of Gases and Liquids*, John Wiley & Sons, Hoboken, NJ.
- [31] Woods, W. W., 1961, "Existence of Detonation for Small Values of the Rate Parameter," *Physics of Fluids*, **4**, pp. 46-60.
- [32] Woods, W. W., 1961, "Existence of Detonation for Large Values of the Rate Parameter," *Physics of Fluids*, **6**, pp. 1081-1090.

VITA

Name: Tetsu Nakamura

Permanent Address: 2-17-14 Nakao Minami-ku, Fukuoka, Japan 811-1364

Email Address: tnakamu2@neo.tamu.edu, eadership@hotmail.com

Education: B.S., Aerospace Engineering, Texas A&M University, 2007

M.S., Aerospace Engineering, Texas A&M University, 2010